Nanotechnology, Science and Applications

Dovepress
open access to scientific and medical research

Open Access Full Text Article

ORIGINAL RESEARCH

Water-Soluble Chitosan Conjugated DOTA-Bombesin Peptide Capped Gold Nanoparticles as a Targeted Therapeutic Agent for Prostate Cancer

This article was published in the following Dove Press journal:
Nanotechnology, Science and Applications

Theeranan Tangthong[1,2]
Thananchai Piroonpan[2]
Velaphi C Thipe[3,4]
Menka Khoobchandani[4,5]
Kavita Katti[4,5]
Kattesh V Katti[4–6]
Wanvimol Pasanphan[1,2]

[1]Department of Materials Science, Faculty of Science, Kasetsart University, Chatuchak, Bangkok, 10900, Thailand; [2]Center of Radiation Processing for Polymer Modification and Nanotechnology (CRPN), Faculty of Science, Kasetsart University, Chatuchak, Bangkok, 10900, Thailand; [3]Laboratório de Ecotoxicologia - Centro de Química e Meio Ambiente - Instituto de Pesquisas Energéticase Nucleares (IPEN) - Comissão Nacional de Energia Nuclear-IPEN/CNEN-SP, São Paulo, Brasil; [4]Institute of Green Nanotechnology, University of Missouri, Columbia, MO, 65211, USA; [5]Department of Radiology, University of Missouri, Columbia, MO, 65211, USA; [6]Department of Physics, University of Missouri, Columbia, MO, 65211, USA

Correspondence: Wanvimol Pasanphan
Department of Materials Science, Faculty of Science, Kasetsart University, 50 Ngam Wong Wan Road, Lat Yao, Chatuchak, Bangkok, 10900, Thailand
Tel +66 2562 5555 (Ext. 646518)
Email wanvimol.p@ku.ac.th

Kattesh V Katti
Institute of Green Nanotechnology, University of Missouri, Columbia, MO, 65211, USA
Tel +1 573 882-5656
Fax +1 573 884-5679
Email KattiK@health.missouri.edu

Introduction: Functionalization of water-soluble chitosan (WSCS) nanocolloids with, gold nanoparticles (AuNPs), and LyslLys3 (1,4,7,10-tetraazacyclododecane-1,4,7,10-tetraacetic acid)-bombesin 1–14 (DOTA-BBN) peptide affords an innovative pathway to produce prostate tumor cell-specific nanomedicine agents with potential applications in molecular imaging and therapy.

Methods: The preparation involves the production and full characterization of water-soluble chitosan (WSCS), via gamma (γ) rays (80 kGy) irradiation, followed by DOTA-BBN conjugation for subsequent use as an effective template toward the synthesis of tumor cell-specific AuNPs-WSCS-DOTA-BBN.

Results: The WSCS-DOTA-BBN polymeric nanoparticles (86 ± 2.03 nm) served multiple roles as reducing and stabilizing agents in the overall template synthesis of tumor cell-targeted AuNPs. The AuNPs capped with WSCS and WSCS-DOTA-BBN exhibited average Au-core diameter of 17 ± 8 nm and 20 ± 7 nm with hydrodynamic diameters of 56 ± 1 and 67± 2 nm, respectively. The AuNPs-WSCS-DOTA-BBN showed optimum in vitro stability in biologically relevant solutions. The targeted AuNPs showed selective affinity toward GRP receptors overexpressed in prostate cancer cells (PC-3 and LNCaP).

Discussion: The AuNPs-WSCS-DOTA-BBN displayed cytotoxicity effects against PC-3 and LNCaP cancer cells, with concomitant safety toward the HAECs normal cells. The AuNPs-WSCS-DOTA-BBN showed synergistic targeting toward tumor cells with selective cytotoxicity of AuNPs towards PC-3 and LNCaP cells. Our investigations provide compelling evidence that AuNPs functionalized with WSCS-DOTA-BBN is an innovative nanomedicine approach for use in molecular imaging and therapy of GRP receptor-positive tumors. The template synthesis of AuNPs-WSCS-DOTA-BBN serves as an excellent non-radioactive surrogate for the development of the corresponding ^{198}AuNPs theragnostic nanoradiopharmaceutical for use in cancer diagnosis and therapy.

Keywords: DOTA-bombesin, gold nanoparticle, water-soluble chitosan, nanoradiopharmaceutical, prostate cancer

Introduction

Green nanotechnology is a promising approach for biomedical applications, such as drug delivery systems, imaging, and therapy.[1–3] Functionalized nanosized particles, due to their size and selective affinity towards tumor cell receptors, possess attractive capabilities to detect, image, or treat tumors/cancers at cellular levels.[4]

submit your manuscript | www.dovepress.com
DovePress
http://doi.org/10.2147/NSA.S301942

Gold nanoparticles (AuNPs) have gained considerable prominence in clinical applications over other metallic nanoparticles primarily because of their biocompatibility[5] relatively lower-toxicity,[6] favorable physio-chemical,[7] and optical properties.[8] Additionally, AuNPs are capable of strong and tunable attenuation of light that provide unique capabilities for the conversion of light to heat – photothermal therapy, and also in the attenuation of X-rays – radiation therapy.[9] Due to these properties, AuNPs have been proposed as contrast agents in X-ray computed tomography (CT) and also as anticancer drug nanocarrier agents for both diagnosis and therapy.[10] Another example where AuNPs continue to gain prominence over other types of metallic/non-metallic nanoparticles is their ability to serve as dual diagnostic and therapeutic agents, thus opening an attractive new avenue of theragnostic in medicine.

Recent investigations by Katti et al have demonstrated the realistic potential of radioactive counterparts of gold metal (such as ^{198}Au and ^{199}Au isotopes) and particularly their nanoparticles (^{198}AuNPs) for use as ideal nanoplatforms for their applications as theranostic nanoradiopharmaceuticals.[11–13] The development of a ready-to-use nanoplatform, for the green synthesis of tumor-targeted AuNPs, is an important strategy toward cancer cell-targeted AuNPs to achieve reduced side effects. The use of engineered AuNPs, having sizes ranging around 85–100 nm, with capabilities of penetrating leaky and porous tumor vasculatures (200–350 nm)—would enable homogenous distribution of therapeutic/diagnostic doses within tumor microenvironment and thereby allow uniform tumor dosimetry.[12] It is known that AuNPs, based on their size, would provide several thousands of gold atoms on their surface. Therefore, if the specific targeted AuNPs are administered into cancer patients, functionalized AuNPs efficiently deliver optimal therapeutic payloads within cancer cells causing effective treatment as compared to free Au ions.

Numerous techniques have been used to prepare AuNPs, which include chemical reduction,[14] sonochemical,[15] photochemical,[16] and radiochemical[17] syntheses. In recent years, research on the synthesis of nanoparticles using "zero carbon emission" green nanotechnology has gained considerable prominence.[18,19] AuNPs production through green nanotechnology involves the application of high-antioxidant capacity phytochemicals as reducing agents to transform gold salts (Au^{3+}) into their corresponding nanoparticles (Au^0) encapsulated with phytochemicals. In this context, plant extracts,[20] alginate,[21] chitosan,[22] high-oxidant natural chemicals,[19] silk fibroin polypeptide[23] and starch[24] have been reported as dual reducing and stabilizing agents for the production of gold nanoparticles.[25] However, biomacromolecules themselves exhibit low reactivity to reduce metal ions to their corresponding metallic nanoparticles because of their inherently high molecular weight, low solubility, low antioxidant activity and low electronegativity. The molecular chain and size reduction including chemical modification has been reported aimed at improving the solubility of chitosan and also for enhancing antioxidant as well as reducing capacities.[22,26,27] Breaking down the glycosidic linkage between the successive monomers generates additional active sites which subsequently scavenge the free radicals. The short-chain chitosan effectively improves its antioxidant activity due to the provision of sufficient spatial extent to form a regular helical structure exposing more hydroxyl groups to the surface of its helical structure—thus resulting in effective bioactivity.[28]

We have developed water-soluble chitosan (WSCS) nanocolloids with the sole objectives of capitalizing on their antioxidant activity as well as in taking advantage of high reducing power to produce functionalized AuNPs for biomedical applications.[17] CS comprises D-glucosamine and N-acetyl-D-glucosamine linked by β (1, 4)-glycosidic linkages. It also exhibits good biocompatibility, biodegradability, low toxicity, and multiple chemical functionalities which can be used to bind to target specific peptides as well as for encapsulation around AuNPs. The amino ($–NH_2$) and hydroxyl (–OH) groups of CS show strong metal ion chelation, antimicrobial and antioxidant properties.[29] Chitosan's antioxidant or reducing –OH, $–NH_2$, and –COOH groups serve as reservoirs of electrons for the transformation of metal salts into their corresponding nanoparticles. The high electron density of electron lone pairs is afforded through the nitrogen and oxygen atoms in the $–NH_2$, –OH, and –C–O–C–including C=O functions, WSCS effectively stabilizes the highly cationic AuNPs surface to prevent their agglomeration.[22] It is quite clear that WSCS plays an important role as a reducing agent; however, the exact mechanism of the reduction process has remained unclear. Previous reports have suggested that -OH and -NH_2 groups of CS would serve as effective reducing agents through electron transfer or hydrogen atom transfer mechanisms.[27,30] CS is well known for its strong metal-ion chelating ability as it has been reported for its natural product antioxidant properties in the deactivation

of catalytic activity of various metal ions.[27] It is also important to note that glucose is a reducing sugar, and it has been used as a reducing agent in the preparation of metal nanoparticles. Chitosan is a polysaccharide and when it is hydrolyzed or depolymerized, it will result in smaller units such as D-glucosamine, a derivative of glucose.[31] In this work, we have used WSCS as a low molecular weight fragment of CS, prepared from the radiation-induced depolymerization. Our approach encompassed utilizing the reduction ability of glucose and other functionalities of WSCS. For example, the -CH-OH (at C-3), -CH_2-OH (at C-6), and -NH_2 (at C-2) groups within the molecular framework of CS may also act as reducing groups in the formation of AuNPs. Therefore, WSCS nanocolloids represent promising water-based biopolymers exhibiting extraordinary antioxidant, reducing, and stabilization abilities—all offering innovative "Zero Carbon Emission" template domain for the effective synthesis of stable AuNPs in neutral media for biomedical applications.

In order to achieve effective targeting of AuNPs toward tumor cell receptors, it is essential to decorate AuNPs with specific peptides possessing well-defined tumor cell specificity and selectivity. Bombesin (BBN) is a 14-amino acid peptide showing high affinity for the gastrin-releasing peptide (GRP) receptors, which are overexpressed in breast, prostate, non-small cell lung cancers, and a host of mammalian tumors.[32] Recently, BBN labeled with radioisotopes, such as ^{99m}Tc, and ^{68}Ga, have been used for the development of tumor-targeted Single Photon Emission Computed Tomography (SPECT)[33,34] as well as Positron Emission Tomography (PET)[35] molecular imaging agents. BBN functionalized on AuNPs has been reported to increase uptake efficiency through targeting of the GRP receptors overexpressed in prostate tumor.[3] BBN conjugated with Lys1Lys3 (1,4,7,10-tetraazacyclododecane-1,4,7,10-tetraacetic acid chelator, DOTA) (DOTA-BBN) has been developed for labeling radioisotopes, such as ^{64}Cu and ^{177}Lu, for clinical translation.[36,37] DOTA-BBN conjugated onto trimethyl chitosan has been proposed for subsequent conjugation with superparamagnetic iron oxide nanoparticles (SPIONs) for applications as magnetic resonance imaging (MRI) for breast cancer diagnosis.[38] Overall, the aforementioned approaches allow the creation of targeted nanoradiopharmaceuticals to enhance diagnostic and therapeutic efficacies of various types of human cancers with minimal side effects to surrounding normal cells/tissues.

The unique chemical architecture of the nanomedicine agent, as described herein, highlights an innovative template synthesis of prostate tumor cells receptor-targeted gold nanoparticles (AuNPs) with optimum in vitro stability. We show that prostate tumor avidity is afforded through conjugation of water-soluble chitosan (WSCS) with the bombesin (BBN) peptide which has selective affinity towards gastrin-releasing peptide (GRP) receptors in vivo that are overexpressed in prostate carcinoma. AuNPs-WSCS-DOTA-BBN are synthesized through an ingenious redox pathway, which uses the high antioxidant capacity of chitosan to inject electrons into the gold precursor to produce water-soluble (WSCS) encapsulated gold nanoparticles in 100% reproducible reactions. The fact that our process does not require any external reducing agent or chemicals to stabilize nanoparticles against agglomeration, in the production of AuNPs-WSCS-DOTA-BBN, is a substantive departure from traditional nanoparticle production schemes. WSCS serves multiple roles of a chemical reductant, encapsulant to stabilize AuNPs, and provides an ideal platform to combine the therapeutic power of AuNPs with the targeting abilities of the conjugated bombesin peptide—all within the new nanomedicine agent AuNPs-WSCS-DOTA-BBN. In this paper, we describe (i) the conjugation of DOTA-BBN peptide with the water-soluble chitosan biopolymer nanocolloids; and (ii) details on the successful optimization of the template synthesis and characterization of BBN conjugated targeted AuNPs. Additionally, we describe: (a) New protocols for characterizing and quantifying the DOTA-BBN-conjugated-WSCS products; (b) Long-term shelf life storage; (c) Specific targeting characteristics and cellular internalization of AuNPs-WSCS and AuNPs-WSCS-DOTA-BBN toward two types of human prostate cancer cell lines (PC-3 and LNCaP); and finally (d) Cytotoxic effects of AuNPs on prostate carcinoma cells with details on nonspecific uptake AuNPs-WSCS for possible toxic effects.

Materials and Methods

Chemicals and Materials. Chitosan with a percent degree of deacetylation (%DD) of 80 (M_w = 258,800 Da) was obtained from Sea fresh Chitosan (Lab) Co. Ltd. (Thailand). Lys1Lys3 1,4,7,10-tetraazacyclododecane-1,4,7,10-tetraacetic acid)-Bombesin 1–14 (DOTA-BBN) was obtained from CSBio Co., Ltd. (USA). 1-Ethyl-3-(3′-dimethylaminopropyl) carbodiimide hydrochloride (EDC) was acquired from Tokyo Chemical Industry (TCI) Co.,

Ltd. (Japan). N-Hydroxysuccinimide (NHS) was obtained from Tokyo Kasei Kogyo Co., Ltd. (Japan). Gold(III) chloride solution ($HAuCl_4$) was purchased from Sigma-Aldrich Corp. (USA). Sodium hydroxide (NaOH) was bought from Carlo Erba Reagent (Italy) and acetic acid (CH_3COOH) was purchased from Lab Scan, Co., Ltd. (Thailand). Aqueous sulfur (S) standard solution (1000 mg/L) with high purity of H_2SO_4 and water was purchased from Sigma-Aldrich Corp. (USA). Dialysis membrane (MWCO = 1000Da) was purchased from Membrane Filtration Products, Inc. (USA). Bovine serum albumin (BSA) and human serum albumin (HSA) were purchased from Sigma-Aldrich, (USA). DL-cysteine and L-histidine were bought from Acros Organics. Sodium chloride (NaCl) and phosphate buffer solutions (pH 5, 7, and 12) were procured from Fisher Scientific (USA). Roswell Park Memorial Institute Medium (RPMI), MTT (3-(4,5-dimethylthiazol-2-yl)-2,5 diphenyl tetrazolium bromide)), dimethyl sulfoxide anhydrous (DMSO), wheat germ agglutinin (WGA), and 1X Dulbecco's Phosphate Buffered Saline (DPBS) were obtained from Sigma-Aldrich (USA). Fetal bovine serum and (FBS) and TryplE were purchased from Gibco BRL (USA). Paraformaldehyde (PFA) was bought from Electron Microscopy Sciences. Gentamicin antibiotic was from APP Pharmaceuticals LLC. Cell lines: prostate cancer cells (PC-3, LNCaP) and human primary aortic endothelial cells (HAECs) cells were obtained from the American Type culture Collection (ATCC; Manassas, VA). PC-3 and LNCaP cells were maintained in 1X RPMI-1640 medium (ATCC® 30–2001™) supplemented with 25 mM D-glucose, 10 mM HEPES, 1 mM sodium pyruvate, 17.8 mM sodium bicarbonate, 2 mM L-glutamine, and 10% fetal bovine serum (FBS) and 14% gentamicin. HAEC cells were maintained in Vascular Cell Basal Medium (ATCC® PCS-100-030™) supplemented with Endothelial Cell Growth Kit-VEGF (ATCC® PCS-100-041™). All pure water with a resistivity of 18.2 MΩ cm was purified by Milli-Q Academic purification set from Millipore.

Instruments and Characterization

Gamma irradiation was carried out using a ^{60}Co source from Gamma Cell 220 irradiator with an absorbed dose rate of 3.3 kGy/h. Chemical structure was characterized using Fourier transform infrared spectrophotometer (FT-IR) and FT-IR spectra were recorded by a Tensor 27 Bruker spectrophotometer with 32 scans at 2 cm^{-1} resolution in a frequency range of 4000–400 cm^{-1}. The elemental composition of the conjugated DOTA-BBN was analyzed using scanning electron microscope with energy-dispersive X-ray spectroscopy (SEM/EDX), FET QUANTA 450 (Netherlands). Sulfur (S) standard addition method was used for quantifying the amount of DOTA-BBN conjugated on WSCS. The standard S solution with different concentrations of 0, 0.02, 0.04, 0.06, 0.08 and 0.10 μg/mL were mixed with WSCS and WSCS-DOTA-BBN solution (7.5 μg/mL, 25 μL) for preparing a set of S standard concentrations. The set of sample solution containing different S standard concentrations was dropped onto copper grid for SEM-EDX measurement. The UV-vis absorption spectra were observed by UV-vis spectrophotometer using a 1-cm path length quartz cuvette with Varian Cary 50 UV-Vis spectrophotometer, Shimadzu (USA). Particle morphologies and sizes were observed by transmission electron microscope (TEM) taken on JEOL JEM-1400 TEM at 120 kV. The samples were centrifuged at 15,000 rpm at 15°C for 15 mins. After spinning was complete, the supernatant was removed and the solution was brought to be an initial volume using deionized water. The sample was sonicated before dropping onto a carbon-coated copper grid (200 mesh × 125 μm pitch). The samples were dried in ambient temperature before TEM measurement. Hydrodynamic diameters and zeta (ζ) potentials were measured using Zetasizer Nano S90, Malvern Instruments Ltd. (USA). Powder X-ray diffraction (XRD) patterns were collected between 51 and 451 2θ in a Bruker AXS (Germany) with CuKα radiation as an X-ray source operating at 50 kV and 100 mA. Small angle X-ray scattering (SAXS) was performed at a small/wide-angle X-ray scattering beam line, BL1.3W, maximum photon energy of 9 keV with 165 mm diameter CCD (Mar SX165) and Mar 345 Image Plate, supported by the Synchrotron Light Research Institute (SLRI), Thailand. Elemental composition was characterized using X-ray photoelectron spectroscopy (XPS) and was carried out at the photoemission spectroscopy (PES) beam line, BL3.2a supported by SLRI, Thailand. Cellular internalization was investigated using Confocal Laser Scanning Microscope from Leica Microsystems (USA). Cytotoxicity studies were investigated using SpectraMax M2 microplate reader from Molecular Devices LLC (USA). Bright-Field CytoViva Hyperspectral Microscopy (CytoViva, Inc. USA). In vitro migration assay was observed using a microscope and images were imported into cellSens Dimension digital imaging software V2.3 (Olympus, Center Valley, PA, USA).

Preparation of Water-Soluble Chitosan Nanoparticles (WSCS)

WSCS was originally prepared according to the procedure described in our previous work.[22] Briefly, CS (10 g) in aqueous acetic acid solution (1% v/v, 1000 mL) was γ-rays irradiated with an absorbed dose of 80 kGy under ambient temperature in air. The samples were neutralized by precipitation in NaOH solution (1% w/v, 600 mL). The sample was dialyzed in a dialysis bag (MWCO = 1000 Da) in deionized water for 24 h. After dialysis, the clear solution was frozen and lyophilized to obtain water-soluble chitosan nanoparticle (WSCS) powder and stored for further characterization.

Bioconjugation of WSCS with DOTA-BBN

WSCS (10 mg) was dissolved in deionized water and stirred overnight to obtain clear solution of WSCS (1 mg/mL, 10 mL). EDC (1.14 mg, 1 mol equiv. to WSCS) was added into DOTA-BBN (11.78 mg, 1 mol equiv. to WSCS) in deionized water (1 mL). NHS (0.68 mg, 1 mol equiv. to WSCS) was then added into the mixture. The reaction was stirred in an ice bath for 15 min. The WSCS aqueous solution (1 mg/mL, 1 mL) was added. The conjugation reaction was further carried out in an ice bath for 6 h. The sample was dialyzed (MWCO = 3500) in deionized water at room temperature for 24 h with magnetic stirring. The product was lyophilized to obtain conjugated product of WSCS-DOTA-BBN and stored for further characterization.

One-Pot Template Synthesis of AuNPs Using WSCS-DOTA-BBN

The WSCS and WSCS-DOTA-BBN powder was dissolved in deionized water and stirred overnight to achieve homogeneous solution. A series of WSCS-DOTA-BBN aqueous solution (0, 1.0, 2.0 and 4.0 mg/mL, 1 mL) was mixed with $HAuCl_4$ aqueous solution (1.0 mM, 1 mL). The mixtures were left for 0, 24, 48, 72, and 96 h at room temperature to obtain different AuNPs samples. Similarly, A series of WSCS aqueous solution was mixed with $HAuCl_4$ aqueous solution at the same protocol. The UV-vis absorption spectra of the AuNPs prepared in WSCS and WSCS-DOTA-BBN aqueous solution were measured using UV-vis spectrophotometer in the absorption range of 500–700 nm.

In vitro Stability Assessment of AuNPs

In vitro stabilities of the AuNPs-WSCS and AuNPs-WSCS-DOTA-BBN were carried out in the biologically relevant solutions: 1% NaCl, 0.5% DL-cysteine, 0.2 M L-histidine, 0.5% bovine serum albumin (BSA), 0.5% human serum albumin (HSA), and phosphate buffer with different pH values (pH 5, pH 7, and pH 12) including deionized (DI) water. The AuNPs-WSCS-DOTA-BBN aqueous solution was prepared using $HAuCl_4$ (1.0 mM, 10 mL) and WSCS-DOTA-BBN (3.0 mg/mL, 10 mL), and the mixture was left for 72 h to obtain stationary state of AuNPs-WSCS-BBN stock solution. The aqueous solution of 1 mL AuNPs-WSCS-BBN (0.5 mM $HAuCl_4$ in 1.5 mg/mL WSCS-DOTA-BBN) was added into each biological fluid (1 mL). The mixtures were incubated for 24 h before recording the UV-vis absorption spectra and their maximum absorption signals using UV-vis spectrophotometer. The hydrodynamic diameters and zeta potentials of AuNPs-WSCS-BBN were measured using DLS.

Cellular Internalization

The human prostate cancer cell line (PC-3 and LNCaP) was seeded with a concentration of 4×10^4 cells/mL into 6-well plates in media RPMI-1640 medium, allowed to adhere for 24 h in CO_2 incubator at 37°C. The AuNPs (50 μg/mL) were added to cells and incubated at 37°C for 24 h. The cells were washed twice with PBS, trypsin, and pelleted down by centrifugation. The cell pellet was then washed with PBS followed by fixation in 2% glutaraldehyde in sodium cacodylate buffer (0.1 M). The cells were further fixed with 1% buffered osmium tetroxide in 0.1 M PBS for 1 h and then dehydrated through a graded ethanol solution. The prepared samples were examined on a confocal laser scanning microscope. In addition, the sample was cut into thin sections using a diamond knife (Diatome, Hatfield PA) and the prepared samples were examined on TEM microscope.

Cytotoxicity of AuNPs

Human prostate cancer cell lines (PC-3 and LNCaP) were sub-cultured in RPMI-1640 medium. HAECs were cultured in Vascular Cell Basal Medium supplemented with Endothelial Cell Growth Kit-VEGF. The cells were stored in CO_2 incubator at 37°C in tissue culture flasks. A concentration of 4×10^4 cells per/mL was seeded into 96-well plate. The cells were incubated overnight to allow cells adherence onto the surface of the plate and the medium was then removed. Thereafter, the cells were

treated with different concentrations of AuNPs-WSCS-DOTA-BBN (6.25, 12.5, 25, 50, and 100 μg/mL). The samples were incubated for 24 and 48 h. Cellular morphologies were investigated using bright-field microscopy. After cellular investigation, MTT dye in PBS solution (5 mg/mL, 10 μL) was added in to the cell samples and incubated at 37°C for 3 h. After incubation, the formed formazan crystals were dissolved using 100 μL of DMSO into the plates and the sample was further incubated for 20 min. The absorbance of the plates was read at a wavelength of 570 nm using SpectraMax M2 microplate reader. The chemotherapeutic drug cisplatin was also used as a positive control.

In vitro Migration Assay (Wound-Healing Assay)

The HAEC cells were suspended in growth medium Vascular Cell Basal Medium supplemented with Endothelial Cell Growth Kit-VEGF. The HAECs (4×10^4 cells/well) were seeded in petri dishes and allowed to grow up to 95% confluent monolayer. Wounds were created using a sterile pipette tip by scratching on the monolayer. Cell debris was removed by washing the cells twice with 1X PBS. The HAEC cells were incubated with chemotherapeutic drug cisplatin (positive control), growth medium (negative control), and treatment groups with AuNPs-WSCS and AuNPs-WSCS-DOTA-BBN (50 μg/mL). The zone of wound healing was observed at 24 h using a microscope. Images were imported into cellSens Dimension digital imaging software V2.3.

Results and Discussion

Conjugation of WSCS Biopolymer Nanocolloid with DOTA-BBN

Our synthetic route of WSCS-DOTA-BBN nanocolloid and its template synthesis of AuNPs are shown in Scheme 1. As facilitated by the chemical structure of WSCS, the –OH and $–NH_2$ groups of WCS react with -COOH on DOTA-BBN. EDC interaction provides the reactive ester intermediate species on DOTA, subsequent interaction with the NHS generates a more stable NHS-ester species. The NHS-ester species is used in reactions with $–NH_2$ or –OH groups of WSCS to form stable amide or ester bonds, respectively.

The DOTA-BBN can be conjugated onto WSCS using the $–NH_2$ group present on C-2 or –OH group or at the C-6 and C-3 to form amide or ester linkages. Fourier transform infrared (FT-IR) spectrum of WSCS-DOTA-BBN was compared with that of DOTA-BBN and WSCS (See Figure S1A in supporting Information). The characteristic peaks at 890, 1034, 1080, 1396, 1562, 1630, 2900, and 3350 cm^{-1} was found in the FT-IR spectrum of WSCS attributed to the presence of pyranose ring, C–O–C bridge, C–O, C–N, N–H, C=O, C–H, and O–H stretching bands[12] (Figure S1A(a)). Compared with the FT-IR spectrum of DOTA-BBN (Figure S1A(b)), the FT-IR spectrum of WSCS-DOTA-BBN (Figure S1A(c)) revealed significant new peaks at 1639 cm^{-1} due to a new amide bond formation between carboxylic acid group of DOTA and the $–NH_2$ of the WSCS. Formation of the ester bond was also evident through observations of a peak at 1728 cm^{-1} suggesting that DOTA-BBN is occurring through carboxylic acid group of DOTA and –OH group of WSCS. The conjugation was further confirmed by the disappearance of bands due to C–O on –CO–OH groups of DOTA at 1174 and 1199 cm^{-1} after conjugation. Observation of additional peaks around 713 cm^{-1}, due to the aromatic ring in the BBN, further inferred the conjugation of the peptide. These FT-IR data provide compelling evidence of the successful conjugation of DOTA-BBN onto WSCS. In addition, conjugation often results in change of symmetry due to the formation of new secondary amide (C=O, amide VI) bonds as reflected through peaks at 528 cm^{-1} attributable to a symmetrical C–N–C stretching vibration. The conjugation results based on FT-IR evidence as described above, indeed agreed well with a similar conjugation of BBN onto dendrimer-folate[39] and conjugation of BBN onto poly (lactic-co-glycolic) acid nanoparticles via amide bonds.[40]

^{1}H NMR spectrum of WSCS-DOTA-BBN is shown in Figure S1B. The appearance of the characteristic peaks of the DOTA-BBN was evident. The chemical shift at 7.1 ppm was interpreted as a characteristic proton on the benzene ring (−PhH−) at f position. The chemical shift at 8.3 ppm at k position and 8.4 ppm at c position of the proton at the amide ($-C(O)NH_2$) side group and the amide bond (−C(O)NH−CH−) backbone were observed. WSCS presented all characteristic peaks of the protons at C-1 to C-6 positions. The degree of substitution (DS) of DOTA-BBN on WSCS was calculated from DS (%) = $(I_{H\text{-}c}/H\text{-}c)/(I_{H\text{-}1}/H\text{-}1) \times 100$; where H-c and H-1 are the selective protons on DOTA-BBN and WSCS structures, respectively. The DS of DOTA-BBN on WSCS was determined to be 5.85%.

In order to confirm the conjugation of DOTA-BBN onto WSCS, the presence of sulfur (S) of the DOTA-

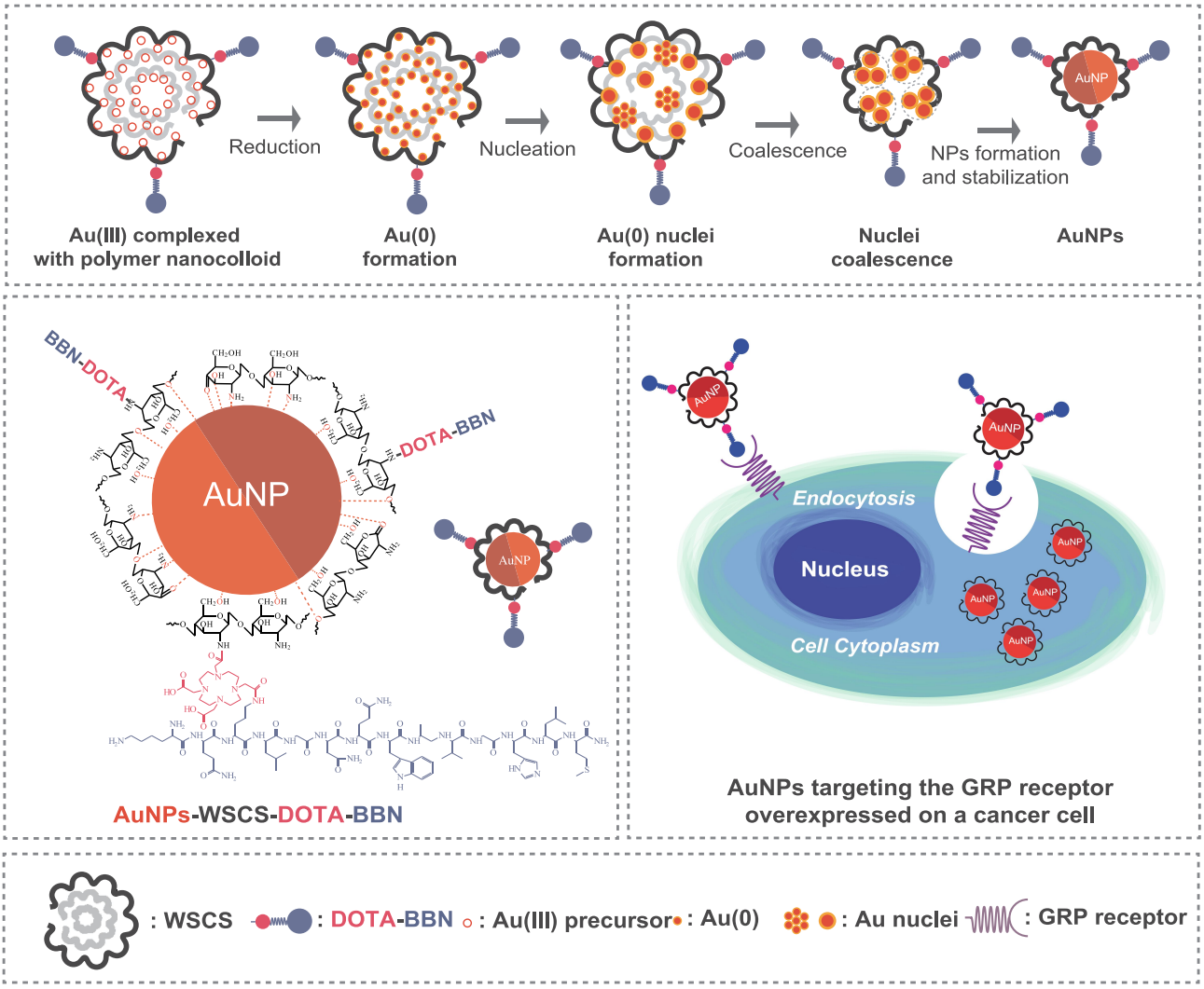

Scheme 1 Possible nanostructured formation of AuNPs via template synthesis using DOTA-bombesin-conjugated-water-soluble chitosan nanocolloids affording targeting functionality of AuNPs to GRP receptors on cancer cells.

BBN structure on the WSCS was measured using X-ray photoelectron spectroscopy (XPS). XPS spectrum of WSCS-DOTA-BBN showed a S_{2p} peak of S (C–S–C) at 168 eV implying the presence of DOTA-BBN moiety on the WSCS (Figure S2 in Supporting Information). Our XPS results of DOTA-BBN conjugated on the WSCS agree well with XPS results of BBN conjugated AuNPs as reported in the literature.[3] The high-resolution XPS peak of the C_{1s} region strongly attests to the presence of N–C=O, C=O, C–O, C–N, and C–C and C–H—all attributed to the conjugated BBN peptide.

Additional confirmation for the conjugation of DOTA-BBN on WSCS has been obtained by measuring the presence of sulfur (S), due to the BBN structure, through SEM-EDX analysis. The S peak was measured from several focal areas under a long-time period measurement with the SEM-EDX. Comparison of the EDX spectrum of the WSCS; WSCS-DOTA-BBN, and DOTA-BBN (Figure 1A(a-c)), respectively, showed a significant EDX peak at an energy of 2.3 keV for the WSCS-DOTA-BBN (Figure 1A(b)) as attributable to a characteristic K_α X-ray of S in the BBN structure compared to the WSCS (Figure 1A(a)). Quantification for the DOTA-BBN moieties, conjugated on the WSCS, was established using standard addition techniques. A series of S standardization was prepared for determining the amount of S in DOTA-BBN present in the WSCS-DOTA-BBN sample (see Figure S3 in supporting information). The amount of DOTA-BBN in the conjugated sample was found to be 32.95% (w/w). The peak due to S and its weight percent found in the SEM-EDX results demonstrated that DOTA-BBN was successfully conjugated with WSCS.

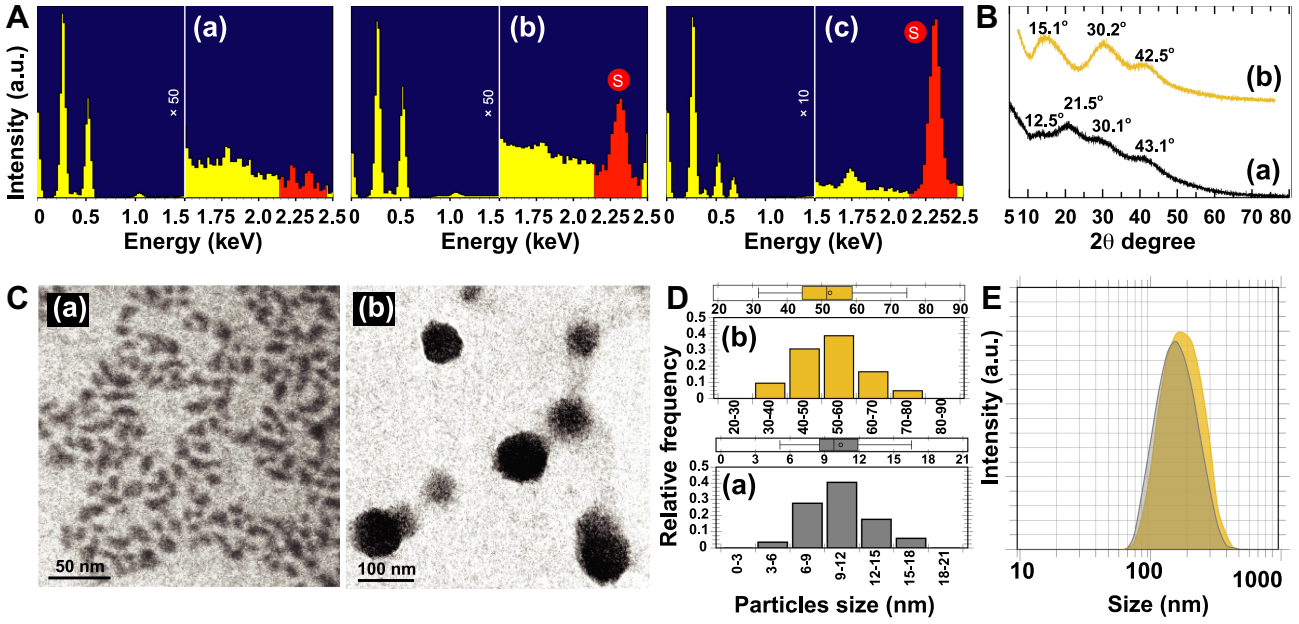

Figure 1 DOTA-BBN peptide conjugated onto WSCS nanocolloids. (**A**) SEM-EDX spectra indicating sulfur elemental composition, (**B**) XRD patterns, (**C**) TEM images, (**D**) particle size distribution calculated from TEM image (n = 200) and (**E**) hydrodynamic size from DLS of (a) WSCS, (b) WSCS-DOTA-BBN and (c) DOTA-BBN.

Powder X-ray diffraction (XRD) patterns of WSCS and WSCS-DOTA-BBN have been recorded in the 2θ angles range of 5° to 80° (Figure 1B). The XRD profile of WSCS shows broad peaks at 12.5 °, 21.5°, 30.2°, and 43.1° 2θ (Figure 1B(a)). The peaks around 12.5 ° and 21.5° 2θ are related to crystal-I and crystal-II of the inter- and intra-molecular hydrogen bonding of chitosan structure.[41] Figure 1B(b) depicts the XRD pattern of WSCS-DOTA-BBN. Significant appearance of a diffraction peak at 15.1° implies the formation of a new crystal due to the conjugated DOTA-BBN segment with concomitant decrease in the crystal-I of WSCS structure at 12.5 ° 2θ. In addition, significant absence of the peak at 21.5° indicates the formation of the conjugated DOTA-BBN thus implying obstruction of hydrogen bonding formation in the crystal-II of WSCS.

Transmission electron microscopy (TEM) was used to determine the morphology of WSCS (Figure 1C(a)) and WSCS-DOTA-BBN (Figure 1C(b)). The particle diameters of the WSCS and WSCS-DOTA-BBN biopolymer nanocolloids were 10 ± 2 and 52 ± 10 nm (Figure 1D(a) and D(b)), respectively. The TEM micrographs revealed a low polydispersity, correlating well with the dynamic light scattering (DLS) measurements. After conjugation with DOTA-BBN, the hydrodynamic diameter (D_H) of WSCS-DOTA-BBN became larger (86 ± 2.03 nm) than that of the original WSCS (49 ± 2.15 nm) (Figure 1E). The zeta potential of the AuNPs formulations was near neutral. The zeta potential of AuNPs-WSCS and AuNPs-WSCS-DOTA-BBN was +1.67 mV and +1.49 mV, respectively. Changes in the morphologies, particle sizes, D_H, and surface charges, as observed, also support the successful conjugation of the DOTA-BBN targeting peptide onto WSCS.

Particle Morphologies and Sizes of AuNPs

The WSCS and WSCS-DOTA-BBB were used as biopolymer nanocolloids template for stabilizing the Au(III) precursor and for subsequent reduction of the Au(III) precursor to Au(0) nanoparticles. The polymer nanocolloids template is expected to control nucleation and growth including coalescence toward the formation of AuNPs (Scheme 1). The WSCS and WSCS-DOTA-BBN, capped on the surface of AuNPs, through electrostatic interactions with the amino ($-NH_2$), hydroxyl (–OH), and carbonyl (C=O) groups of WSCS[22] and their stabilization behavior have been extensively described in the literature.[42] Under almost neutral pH (pH 6.5–7.0) conditions, the Au(III) coordinates on to the deprotonated WSCS main chain of the biopolymer colloidal template. This phenomenon affects AuNPs formation by limiting the amount of Au(III) atoms coordinated on the glucosamine units.[43,44]

The morphologies and particle sizes including crystal structure of the AuNPs were monitored using TEM, SAXS, HR-TEM, and XRD. TEM images of AuNPs-WSCS and AuNPs-WSCS-DOTA-BBN are shown in

Figure 2A(a) and A(b), respectively. Most of the AuNPs, as prepared in WSCS, exhibited spherical-like shape (Figure 2A(a)). The AuNPs-WSCS-DOTA-BBN revealed clear particle formation with several shapes (Figure 2A (b)). Although a majority of nanoparticles are spherical, other shapes (eg, round triangle, diamond, rod, and hexagonal) of AuNPs were also observed in minor quantities especially with WSCS-DOTA-BBN colloid template (Figure S4 in supporting information). We infer that the coalescence of Au crystallites and chemical structural

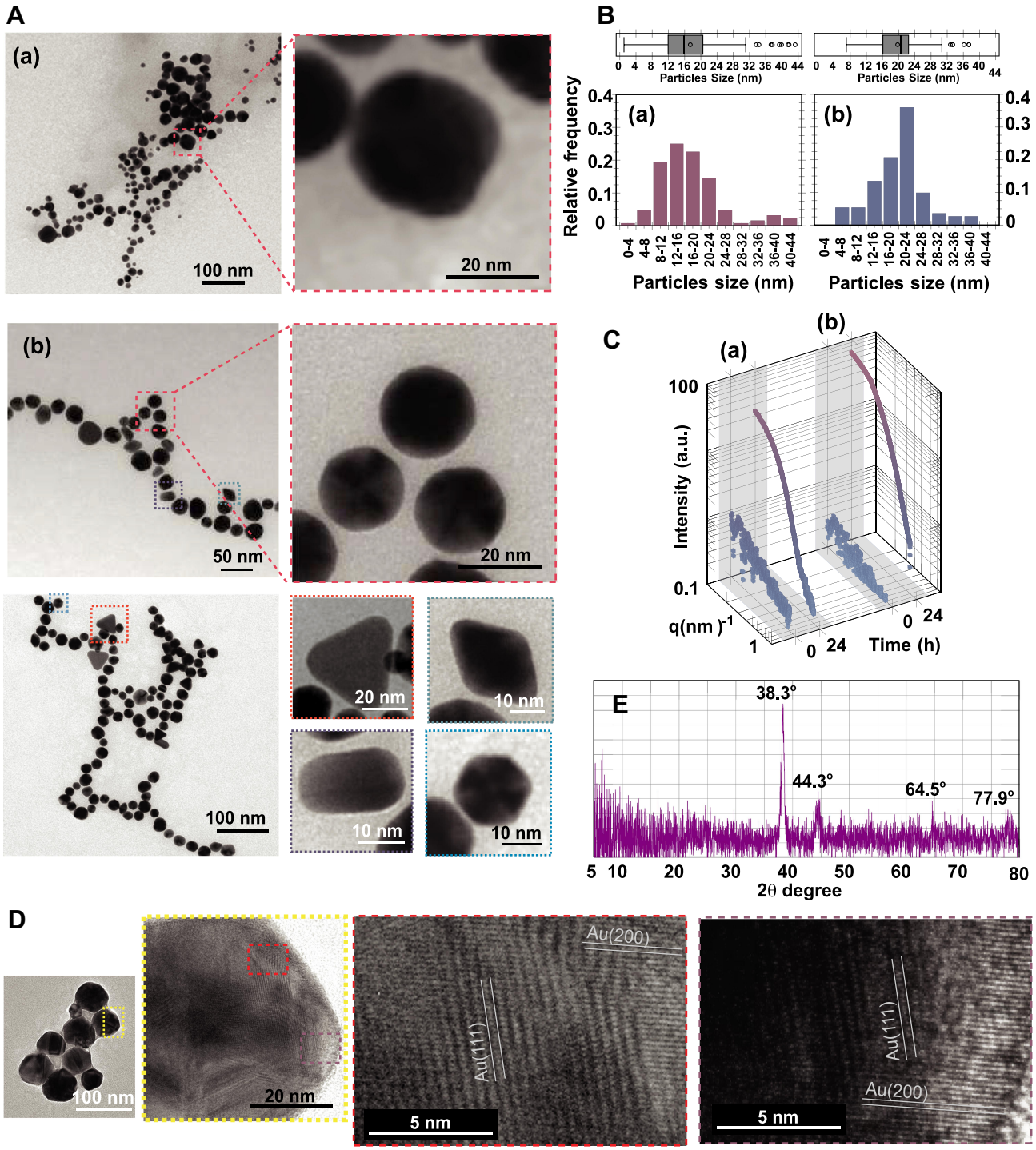

Figure 2 (**A**) TEM images and their close-up images, (**B**) particle size distribution calculated from TEM images (n = 200), and (**C**) SAXS scattering curves at 0 and 24 h of (a) AuNPs-WSCS and (b) AuNPs-WSCS-DOTA-BBN. (**D**) Representative HR-TEM image and close-up image of the Au nanocrystal, showing the (111) and (200) lattice planes. (**E**) Representative XRD pattern of AuNPs as in (b).

templates presumably results in the formation AuNPs with different shapes. The varied shapes of AuNPs are often influenced by polymer template effects comprising linear peptide chain of BBN conjugated on pyranose ring as well as through the polysaccharide chain in WSCS structure. It has been reported that the adsorption of different chemical species on the surface of AuNPs has a very dramatic effect on the surface energy.[44] There is evidence that the formation and structure of smaller nanoparticles are dictated by the ratio of the surface free energy to the total energy.[45] In addition, by changing the surface energies of the crystal faces, it is possible to tune the shapes of the particles. Figure 2B shows the size distribution histogram of Au core size of the AuNPs. The Au core size of AuNPs-WSCS and AuNPs-WSCS-DOTA-BBN was 17 ± 8 nm and 20 ± 7 nm (Figure 2B(a) and B(b)), respectively.

The Au-core size was estimated based on the scattering intensity data obtained from Small angle X-ray scattering (SAXS). SAXS scattering curves of AuNPs, prepared in WSCS and WSCS-DOTA-BBN, recorded at an initial state and after 24 h of reaction are shown in Figure 2C(a) and C(b), respectively. The radius of Au-core (R) can be calculated from radius of gyration (R_g) based on the Guinier equation ($R = R_g(5/3)^{1/2}$), where R_g is an indicator for observing how the mass of the particle is distributed around its center of mass. According to SAXS scattering data of AuNPs-WSCS (Figure 2C(a)) and AuNPs-WSCS-DOTA-BBN (Figure 2C(b)), it was found that the Au-core diameter of AuNPs-WSCS and AuNPs-WSCS-DOTA-BBN was 18.25 and 24.06 nm, respectively. The Au-core sizes observed from SAXS agreed well with the nano-dimension and size as estimated from TEM images.

High-resolution TEM (HRTEM) allows resolving the atomic structure of the AuNPs. Figure 2D shows a representative HRTEM image of Au nanostructure obtained from the template synthesis using WSCS-DOTA-BBN. The presence of the crystal lattice planes of the Au nanocrystals provides evidence on the crystallinity of AuNPs. To support the atomic structure of the AuNPs, the XRD pattern of AuNPs-WSCS-DOTA-BBN is shown in Figure 2E. The XRD pattern of AuNPs-WSCS-DOTA-BBN exhibited characteristic diffraction peaks at 38.3°, 44.3°, 64.5°, and 77.9° that can be indexed to the (111), (200), (220), and (311) Bragg's reflections of face-centered cubic (fcc) structure of metallic Au. This pattern indicates typical pure nanocrystals in AuNPs and the XRD patterns matched well with the JCPDS file No. 04–0784.[46] The aforementioned results, taken together, provide unequivocal evidence that the AuNPs in AuNPs-WSCS-DOTA-BBN conjugate are indeed crystalline in nature.

SEM-EDX investigations were further performed in order to confirm that the presence of BBN targeting peptide on the backbone of AuNPs. SEM-EDX provides morphology and elemental composition for mapping. The SEM-EDX image and their nanoscale elemental mapping of the AuNPs-WSCS-DOTA-BBN are shown (Figure 3). Au elemental mapping indicated a characteristic spectrum of Au L_α X-rays at 9.711 keV, whereas S elemental mapping was marked by characteristic spectrum of S K_α X-rays at 2.309 keV. The red color profile reveals the presence of Au element (Figure 3B), while the green profile indicates the presence of S element (Figure 3C) in the BBN structure. As shown in Figure 3D, the AuNPs containing S element on their surface implies that the BBN targeting peptide was anchored with the AuNPs through the WSCS-DOTA-BBN template.

Optimization of AuNPs Formation in WSCS and WSCS-DOTA-BBN

The effects of the concentrations of WSCS and WSCS-DOTA-BBN biopolymer nanocolloids template on the formation of AuNPs were evaluated through the characteristic surface plasmon resonance (SPR) using UV-vis absorption measurements (Figure 4). The AuNPs were

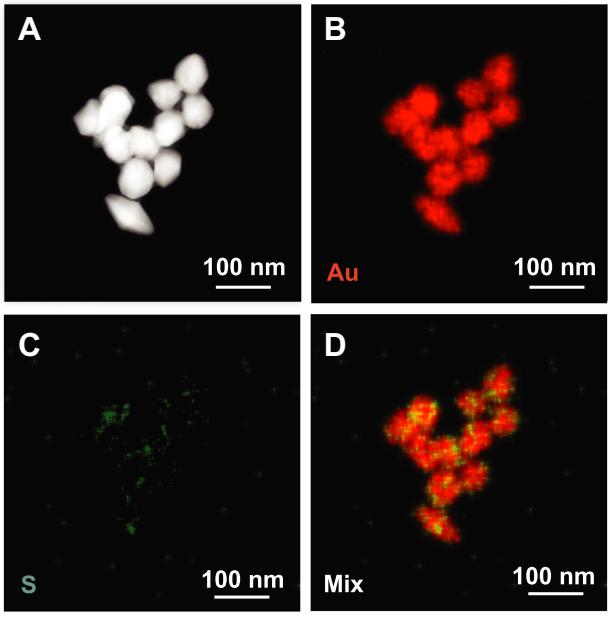

Figure 3 WSCS-DOTA-BBN covering on the surface of AuNPs observed from SEM-EDX. (**A**) SEM image, (**B**) Au, (**C**) S and (**D**) mixed Au and S mappings of the AuNPs-WSCS-DOTA-BBN.

synthesized using 0.5 mM $HAuCl_4$ in the presence of various concentrations (0.5, 1.0, 1.5 and 2.0 mg/mL) of WSCS and WSCS-DOTA-BBN in aqueous solutions. The formation of AuNPs was inferred by their SPR absorptions in the UV-absorption wavelength range of 530–540 nm which is characteristic of nanoparticulate gold formation (see Figure S4(A) in supporting information). The concentration of biopolymer nanocolloids template has a significant influence on the formation of AuNPs. Increases in the WSCS and WSCS-DOTA-BBN concentrations resulted in increases in the SPR absorption. The physical appearance, corresponding to each concentration, is also presented below through relative plots. More intense pink color was attributed to high UV absorption intensity. The SPR absorptions subsequently level off when the concentrations reached saturation. The changes of UV extinction coefficients (absorption intensities) indicate the concomitant changes in the yields of AuNPs produced in each of the systems. The yield and the numbers of AuNPs increased by increasing the concentration of biopolymer nanocolloids template, acting as reducing and stabilizing agents, used in the reactions. The SPR absorption of AuNPs, prepared via WSCS and WSCS-DOTA-BBN, remained in steady state within the concentration ranges of 1.0–1.5 mg/mL. These experimental results suggested that the optimum concentrations of biopolymer nanocolloids template were in the range of 1.0 to 1.5 mg/mL. The SPR adsorption of AuNPs, prepared via WSCS-DOTA-BBN (Figure 4A(b)) was lower than that of AuNPs prepared in WSCS (Figure 4A(a)). It may be noted that the conjugation of BBN onto polyethylene glycol (PEG), capped on AuNPs, changes the SPR of AuNPs to red shift or a longer wavelength. BBN binding changes the local environment thus resulting in significant changes in SPR absorption of PEG-AuNPs.[47]

The D_H and zeta potential of AuNPs, prepared using various concentrations of WSCS and WSCS-DOTA-BBN, were measured using DLS (Figure 4A). The D_H increased with increasing reaction time. The D_H of AuNPs-WSCS-DOTA-BBN was 42 ± 1, 62 ± 2, 67 ± 2, and 116 ± 5 nm at concentrations of 0.5, 1.0, 1.5 and 2.0 mg/mL, respectively (Figure 4A(b)). In contrast, the D_H of AuNPs-WSCS was slightly smaller (Figure 4A(a)). The D_H of AuNPs-WSCS-DOTA-BBN was higher due to the conjugated BBN hydrophilic segment capped on the AuNPs surface. A similar result has been noted for lysozyme-albumin and BBN coated AuNPs.[48]

Surface charges of AuNPs in WSCS and WSCS-DOTA-BBN were evaluated in order to gain insights on physiochemical characteristics of various functionalized AuNPs

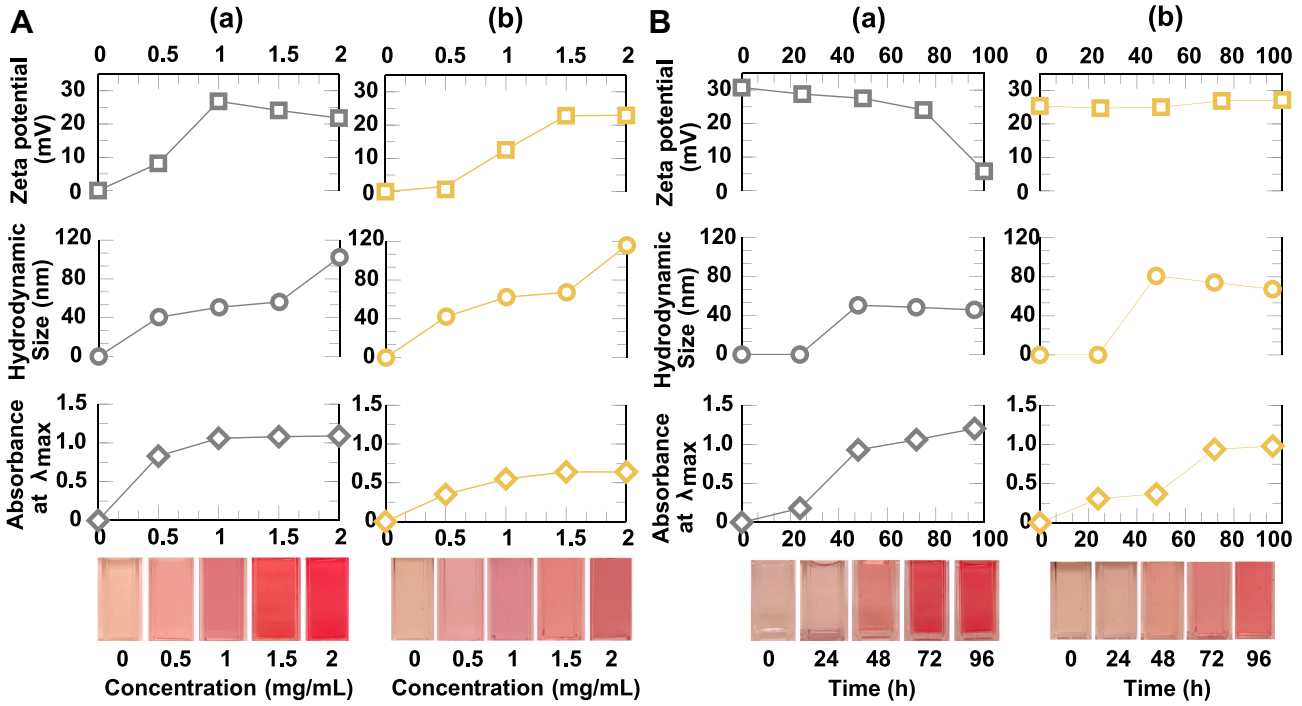

Figure 4 Effects of (**A**) polymer template concentration and (**B**) reaction time on the AuNPs formation in (a) WSCS and (b) WSCS-DOTA-BBN observed via UV-Vis absorption intensities at λ_{max} and corresponding physical appearance (bottom), hydrodynamic sizes, and zeta potentials.

(Figure 4A). At 1.5 mg/mL, the zeta potentials of AuNPs-WSCS and AuNPs-WSCS-DOTA-BBN were measured in the range of +20 to +30 mV implying incipient stability. The positive zeta potential of AuNPs in both WSCS and WSCS-DOTA-BBN solution may be due to an intrinsic surface charge on the AuNPs. Typically, AuNPs have zeta potential greater than +20 mV or less than −20 mV exhibiting sufficient electrostatic repulsion to remain stable in the solution.[49] With the peptide conjugation, WSCS-DOTA-BBN nanocolloids template exhibited zeta potential close to neutral. Therefore, it appears that the surface charge of AuNPs-WSCS-DOTA-BBN is compensated by the BBN peptide conjugated WSCS that are capped on AuNPs. A similar observation has been noted in the case of AuNPs conjugated with the tumor necrosis factor (TNF). The surface charge on the naked AuNPs was −38 mV and the zeta potential shifted to −34.55 mV upon conjugation with TNF.[50]

The effect of reaction times (0–96 h) on the formation of AuNPs was also studied as shown in Figure 4B. The absorption intensity (extinction coefficient), as found in the UV-vis spectra, increased when the reaction times increased (see Figure S5 in supporting information). At 24 h, the SPR absorption and the D_H of AuNPs was quite low and was not observed (Figure S5(A) and (B)). When the reaction durations increased to 48 h, the UV-vis absorption intensities increased significantly. Plots of the reaction times against the UV-vis absorption, D_H and zeta potential are shown in Figure 4(B). The SPR intensity of AuNPs-WSCS significantly increased at 48 h with increases in the reaction time periods from 48 to 96 h (Figure 4B(a)). For the AuNPs-WSCS-DOTA-BBN, the SPR intensity was very high at 72 h and reached a steady state within the reaction time periods of 72–96 h (Figure 4B(b)). The D_H of AuNPs-WSCS and AuNPs-WSCS-DOTA-BBN were 40–50 nm and 60–80 nm within the reaction times of 48–96 h. The zeta potentials of AuNPs-WSCS were around +25 to +30 mV. For AuNPs-WSCS-DOTA-BBN, the zeta potentials were around +25 mV. The zeta potential of AuNPs-WSCS and AuNPs-WSCS-DOTA-BBN provides information on the stability of nanoparticles dispersion within the studied reaction times of 24–96 h. As the zeta potential indicates the quantum of repulsive forces that are present, the magnitude of measured zeta potential can be considered to predict the long-term stability of nanoparticulate dispersions.

A systematic optimization of AuNPs, with optimal hydrodynamic sizes (D_H of ~70 nm) for applications in nanomedicine, has been successfully achieved through the WSCS-DOTA-BBN polymer nanocolloids template (1.5 mg/mL) using $HAuCl_4$ as the precursor (0.5 mM) and employing a reaction time of 72 h. The D_H of AuNPs-WSCS (ca. 60 nm) and AuNPs-WSCS-DOTA-BBN (ca. 70 nm) are approximately 3 times larger than that of the Au-core size of AuNPs (~18 and ~22 nm) as determined by TEM and SAXS. This data also suggests that the AuNPs were coalesced and wrapped within the WSCS and WSCS-DOTA-BBN polymer nanocolloid template as also confirmed through SEM-EDX measurements (Figure 3). The particle sizes of AuNPs capped with WSCS-DOTA-BBN were in the range of optimum particle sizes (10–100 nm).[51]

The interrelationship between reaction durations on the overall long-term in vitro stability of AuNPs for long-term storage applications was investigated. Detailed SPR investigations through UV spectroscopy have inferred that AuNPs in WSCS-DOTA-BBN, synthesized through reaction durations of 72 h, maintain long-term stability for over 1 week under room temperature and 5°C. Full details on the long-term stability of AuNPs at different time points (1 h up to 6 months) were analyzed by monitoring the SPR using UV-visible spectroscopy (see Figure S6 in supporting information).

Vitro Stability of AuNPs in Biological Media

Metallic nanoparticles are susceptible to agglomeration in biological fluids. Due to the surface properties of AuNPs, agglomeration generally happens in biological media under the in vitro and in vivo profiles. We have therefore investigated the in vitro stability of AuNPs in various biologically relevant solutions at different pH using buffer solutions. The in vitro stability of AuNPs-WSCS and AuNPs-WSCS-DOTA-BBN was performed in a set of biological fluids (1% NaCl, 0.5% Cys, 0.2 M His, 0.5% BSA, 0.5% HSA, and buffer with pHs of 5, 7, and 12) as shown in Figure 5A(a-i) and 5B(a-i), respectively. The in vitro stability was monitored via changes of the maximum wavelength (λ_{max}) and D_H, zeta potentials after 24 h.[52] The D_H of AuNPs-WSCS (Figure 5(A)) and AuNPs-WSCS-DOTA-BBN (Figure 5 (B)) were 120–170 nm when incubated in DI (pH 5.5), Cys (pH ~5.0–5.5), His (pH ~7.0–7.5), BSA (pH ~5.8–7.5), and HSA (pH 5.5–7.5) and phosphate buffer solutions at pH 12. The surface charge changed to near neutral (+5 to +10 mV) because of

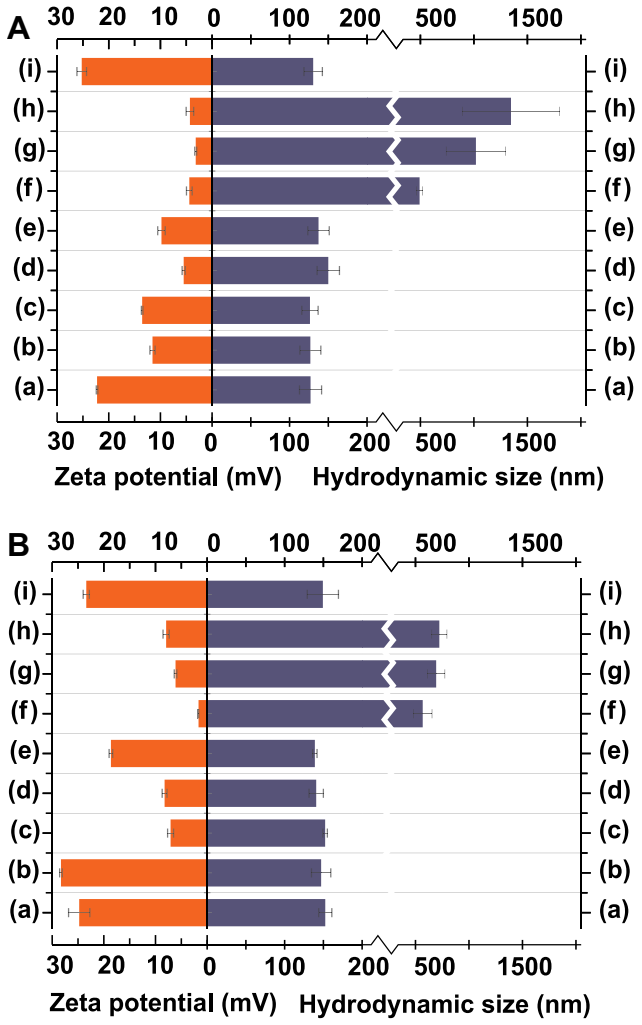

Figure 5 In vitro stability of (**A**) AuNPs-WSCS and (**B**) AuNPs-WSCS-DOTA-BBN in biological relevant solutions: (a) DI, (b) 0.5% Cys, (c) 0.2 M His, (d) 0.5% BSA, (e) 0.5% HSA, (f) 1% NaCl, (g) PBS pH 5, (h) PBS pH 7, and (i) PBS pH 12 after incubation for 24 h.

the charge differences present at the surface of AuNPs and the surrounding media. There is compensation of the positive charge of the proteinogenic amino acids and protein-based biological fluids. Therefore, the stability of AuNPs was somewhat reduced in such biological fluid. In NaCl (1%, pH ~7) and phosphate buffer at pH 5 and pH 7 (Figure 5A(f-h) and 5B(f-h)), the zeta potential also changed to +5 mV and the AuNPs-WSCS (~500-1700 nm) and AuNPs-WSCS-DOTA-BBN (~500-750 nm) became bigger because of particle agglomeration. In the PBS buffer pH 12 (Figure 5(i)), the particle size of AuNPs was ~150 nm and the zeta potential was +25 mV presumably because of the competition of the negative charge of the media and the cationic AuNPs, to compensate for the zeta potential to be more positive, thus resulting in reduced agglomerations. The above results confirm that agglomeration process of the AuNPs depends on the surface charge, chemical composition, and on the pH of the surrounding media.

Cellular Internalization

Development of cancer receptor-specific AuNPs will allow efficient targeting/optimum retention of engineered AuNPs within tumors and thus provide synergistic advantages in oncology as it relates to molecular imaging and therapy. In this work, we have used BBN peptide with well-established high affinity toward GRP receptors that are overexpressed on prostate cancer as well as breast, and small-cell lung carcinoma.[36] Two types of prostate carcinoma cell lines (PC-3 and LNCaP) were used as representative high and low GRP receptor expressing cells, respectively.[53] In order to prove the affinity of the AuNPs-WSCS-DOTA-BBN toward GRP receptors on prostate cancer cells, cellular internalization assays were performed using confocal microscopy and TEM.

Figure 6 shows confocal microscopic and TEM images of the PC-3 cells after exposing them with AuNPs. It is well-known that human prostate tumor PC-3 cells exhibit a large density of GRP receptors on the surface of the cells.[54] Therefore, we are interested in investigating the ability of the AuNPs, capped using the DOTA-BBN conjugated WSCS nanocolloids template, to target GRP receptors and subsequent internalization into the targeted cancer cells. Figure 6(A-C) shows the fluorescence micrograph depicting the cell cytoplasm, nuclei, and AuNPs indicated in green (515 nm), blue (450 nm), and yellow (561 nm) channels, respectively. Figure 6A shows the PC-3 control group (no treatment), while Figure 6B and C shows PC-3 with AuNPs-WSCS and AuNPs-WSCS-DOTA-BBN treatment, respectively. High magnification of cellular internalization indicated presence of a significant amount AuNPs in the PC-3 cells (see (a), (b), and (c) positions in Figure 6). After 2 h treatment, the AuNPs-WSCS-DOTA-BBN, as indicated in yellow, were mostly observed outside the PC-3 cells (data not shown) and some of them were taken into the cell cytoplasm. After incubation for 6 h, a significant amount of AuNPs-WSCS-DOTA-BBN was internalized into the PC-3 cells and localized in the cytoplasm without disturbing the nucleus (Figure 6C). Some amount of AuNPs-WSCS without DOTA-BBN conjugate (Figure 6B) was also found in the PC-3 cells. This may be due to small particle sizes of

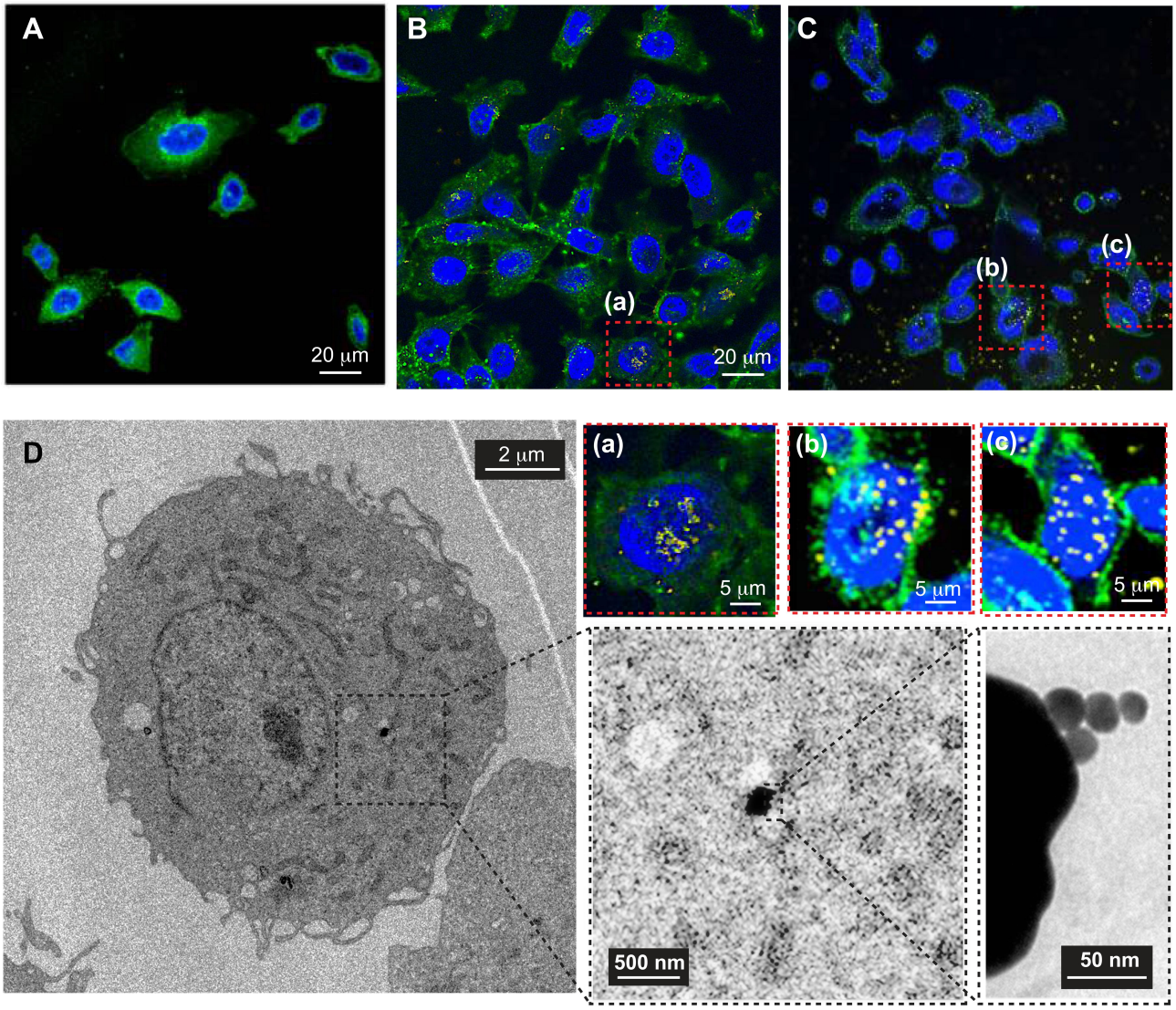

Figure 6 AuNPs depicting internalization into the representative PC-3 prostate cancer cells. (**A**) Confocal microscopic images of PC-3 cells: (**A**) without treatment, (**B**) treated with AuNPs-WSCS, (**C**) treated with AuNPs-WSCS-DOTA-BBN at 6 h, and their corresponding close-up images (bottom) at (a), (b) and (c) positions. (**D**) Representative TEM images and close-up morphologies of (**C**) condition.

both AuNP derivatives allowing them to enter the cells. The endocytosis of AuNPs-WSCS-DOTA-BBN into tumor cells is rationalized in terms of selective and has a natural affinity to bind to the GRP receptors of PC-3 cells thus resulting in significant cell internalization. However, it is also important to note that AuNPs-WSCS, without the peptide conjugate, also showed their ability to enter into the PC-3 cells. This may be due to the cationic characteristic of chitosan, which exerts advantages as a desirable drug carrier due to the enhanced adhesion to the negatively charged mucosal cellular surface, by electrostatic interaction, resulting in drug internalization into the targeted cells.[55] Therefore, the synergistic effects of WSCS function may be beneficial to enhance the targeting ability of AuNPs with the cell surface leading to optimum endocytosis and thereby help in achieving enhanced therapeutic efficacy.

Selective GRP receptor-mediated endocytosis AuNPs-WSCS-DOTA-BBN, within prostate cancer cells, has been unequivocally corroborated through TEM images of cell internalization of AuNPs in to PC-3 cells (Figure 6D). TEM images showed a significant amount of AuNPs within PC-3 cells. The TEM images were also used to gain insights on the morphology and in vitro stability of targeted AuNPs in tumor cells. The nanostructured morphology and particle size of AuNPs (~20 nm) (Figure 6) are very similar to the native AuNPs as depicted in Figure 2. The internalized AuNPs were found to be intact with clear morphology thus confirming

the high in vitro stability of AuNPs-WSCS-DOTA-BBN within the tumor microenvironment. The AuNPs-WSCS-DOTA-BBN also targeted the receptors on LNCaP cell (see Figure S7 in supporting information); however, the extent of endocytosis appears to be significantly lower as compared with the PC-3 cells. The uptake of AuNPs in PC-3 cells is predominantly due to the surface chemistry of the targeted AuNPs correlating to the number of GRP receptor on the cells.[56] Moreover, PC-3 cells express 500-fold more protein receptors with relatively higher GRP receptors than LNCaP cells. GRP receptors immunoreactivity is associated with Gleason score, thus making PC-3 cells as models for highly aggressive prostate cancers as compared to LNCaP cells.[57–59] Additionally, PC-3 and LNCaP cells represent ideal models for studying GRP receptor-mediated molecular targeting, attributed to their GRP receptor differential expression levels (GRP receptor densities for PC-3 and LNCaP are 47,600 and 100 binding sites per cell, respectively). The lower densities of GRP receptors in LNCaP corroborated well with our observations of lower cellular internalization of the AuNPs-WSCS-DOTA-BBN as compared with the PC-3 cells.[60–62]

In general, NPs are taken up from the cell surface through endocytosis and confined to the endosome (Scheme 1). This can occur through either receptor-mediated endocytosis, which are expected for the targeted AuNPs, or through pinocytosis that are known for the nonfunctionalized AuNPs. It is also important to recognize that the particles can avoid the endosomal pathway by being taken up directly into the cytosol using cell-penetrating peptides. However, the BBN peptide is not a cell-penetrating peptide. All of these observations, taken together, we infer that the AuNPs-WSCS-DOTA-BBN are internalized within prostate tumor cells through the receptor-mediated endocytosis mechanism. The highly efficient cellular uptake of these AuNPs demonstrates GRP receptor affinity and selectivity, thus validating our hypothesis on the creation of prostate tumor-specific AuNPs via BBN peptide conjugated WSCS biopolymer nanocolloid template.

Cytotoxicity Studies of AuNPs Against Prostate Cancer

The cellular morphological integrity of the untreated and treated cancer cells (PC-3 and LNCaP) with the AuNPs-WSCS and AuNPs-WSCS-DOTA-BBN (50 μg/mL) under in vitro conditions were investigated through bright-field microscopy at post-incubation periods of 24 and 48 h. Analysis of the effects of AuNPs on cell morphology indicates that morphological shapes of PC-3 and LNCaP cells were drastically changed in a time-dependent fashion (see Figures S8 and S9 in supporting information). Cellular density of the PC-3 and LNCaP decreased, while cellular debris representing cell death was prevalent. The cellular images strongly indicate evidence of apoptotic events, which include surface detachment, deformation of cell bodies, cellular shrinkage and blebbing, nuclear condensation, and nucleus fragmentation. These morphological changes suggest a point-of-no-return apoptotic cancer cells destruction. For example, PC-3 and LNCaP cells were detaching themselves from the surface and changing to a round shape in the treatment groups when observed at 24 h. Increasing the time of incubation showed concomitant increases in the number of cancer cells death. It may be noted that cell apoptosis was more significant when AuNP nanoconjugates of BBN peptide (AuNPs-WSCS-DOTA-BBN) were used as compared to the non-BBN conjugate: AuNPs-WSCS. In all these experiments, the untreated cancer cells (used as controls) proliferated at normal pace; whereas the treated cancer cells were completely destroyed.

In order to further evaluate the target-specific effectiveness of the BBN biofunctionalized AuNPs with GRP receptors of PC-3 and LNCaP cells, their specific interaction and cytotoxicity with cells has been investigated. BBN peptide has a high affinity to GRP receptors that are overexpressed on prostate cancer cells. It is therefore important to ascertain if the BBN peptide functioned on AuNPs-WSCS-DOTA-BBN would still maintain its GRP receptor specificity. For this, we have first studied the cytotoxicity of AuNPs using two types of prostate carcinoma cell lines under in vitro conditions through a colorimetric cell-viability (MTT) assay. In this study, only the viable cells are capable to metabolize a dye (3-(4,5-dimethylthiazol-2-yl)-2,5 diphenyltetrazolium bromide) to produce purple colored crystals which were then dissolved with DMSO and analyzed by spectrophotometry. This experiment was performed using a wide range of AuNPs concentrations (0, 12.5, 25, 50, and 100 μg/mL) and the cells were incubated for 24 and 48 h before measurement. Cytotoxic effects of the AuNPs-WSCS (gray color) and AuNPs-WSCS-DOTA-BBN (yellow color) were observed through cell viability of the PC-3 (Figure 7A) and LNCaP (Figure 7B) cells in a dose-dependence manner. At 24 h (Figure 7A(a) and 7B(a)), the cell viability of PC-3 (≥70%) was higher than that of LNCaP (<70%). However, at a post-incubation time of 24

h, with AuNPs-WSCS (gray color) and AuNPs-WSCS-DOTA-BBN (yellow color), both types of prostate cancer cells showed higher viability than the control tumor cells. For PC-3 cells, after 48 h incubation, the AuNPs-WSCS and AuNPs-WSCS-DOTA-BBN displayed the half maximal inhibitory concentration (IC_{50}) values of 80.41 and 65.89 µg/mL (Figure 7A(b) and 7B(b)), respectively (see Figure S10(A) in supporting information). Similar data demonstrating the role of BBN targeting peptide were also observed in the LNCaP cell lines (see Figure S10(B)). The IC_{50} value for AuNPs-WSCS is >100 µg/mL and IC_{50} value of AuNPs-WSCS-DOTA-BBN was found to be 60.73 µg/mL. At 48 h, the IC_{50} values of AuNPs-WSCS-DOTA-BBN against the PC-3 and LNCaP cell lines remained almost identical. Our results, therefore, have demonstrated that BBN peptide conjugated on the AuNPs-WSCS plays a significant role in targeting the GRP receptor overexpression on the PC-3 and LNCaP cells as illustrated in Scheme 1. It is important to note that the surface charges of AuNPs would exert significant influence on the ability of nanoparticles for effective interaction with cancer cells. For example, the cationic AuNPs can effectively bind the negatively charged DNA of cancer cells. When DNA binds to highly positive AuNPs, it wraps around the NPs ensuing topological bending effects. This type of bending results in effective DNA damage and complete destruction of cancer cells.[63]

Our observations, as discussed above, corroborate with various results from previous studies on the cytotoxicity effects of AuNPs conjugated with various targeting molecules, such as transferrin, folic acid, and aptamer, against prostate cancers. For example, the cytotoxicity of negatively charged polyethylene glycol AuNPs with the transferrin, a serum glycoprotein, targeting ligands (AuNPs-PEG-Tf) and positively charged polyethyleneimine have been reported. In this study, the AuNPs, with the folate-receptor targeting ligands (AuNPs-PEI-FA) against the PC-3 and LNCaP cells have been investigated.[64] It has been reported that IC_{50} of AuNPs-PEG-Tf were 107 and 103 µg/mL and IC_{50} of AuNPs-PEI-FA were 120 and 110 µg/mL for PC-3 and LNCaP cells, respectively. In our investigations, as discussed above, we have observed values of IC_{50} for AuNPs-WSCS-DOTA-BBN as 65.89 and 60.73 µg/mL against PC-3 and LNCaP cells, respectively. Our investigations further indicated that the BBN peptide conjugated WSCS exhibited almost 2 times more toxicity to prostate cancer cells than the previously reported transferrin conjugated PEG and folic acid conjugated PEI. In addition, the aptamer peptide conjugated AuNPs have been proposed for anticancer drug loading toward prostate cancer treatment.[65] Also, the doxorubicin-loaded, prostate-specific membrane antigen (PSMA) aptamer-conjugated AuNPs (10 µM), exhibited lower cell viability of the targeted LNCaP cells (50 ± 6%) than the nontargeted PC-3 cells (71 ± 6%) at 24

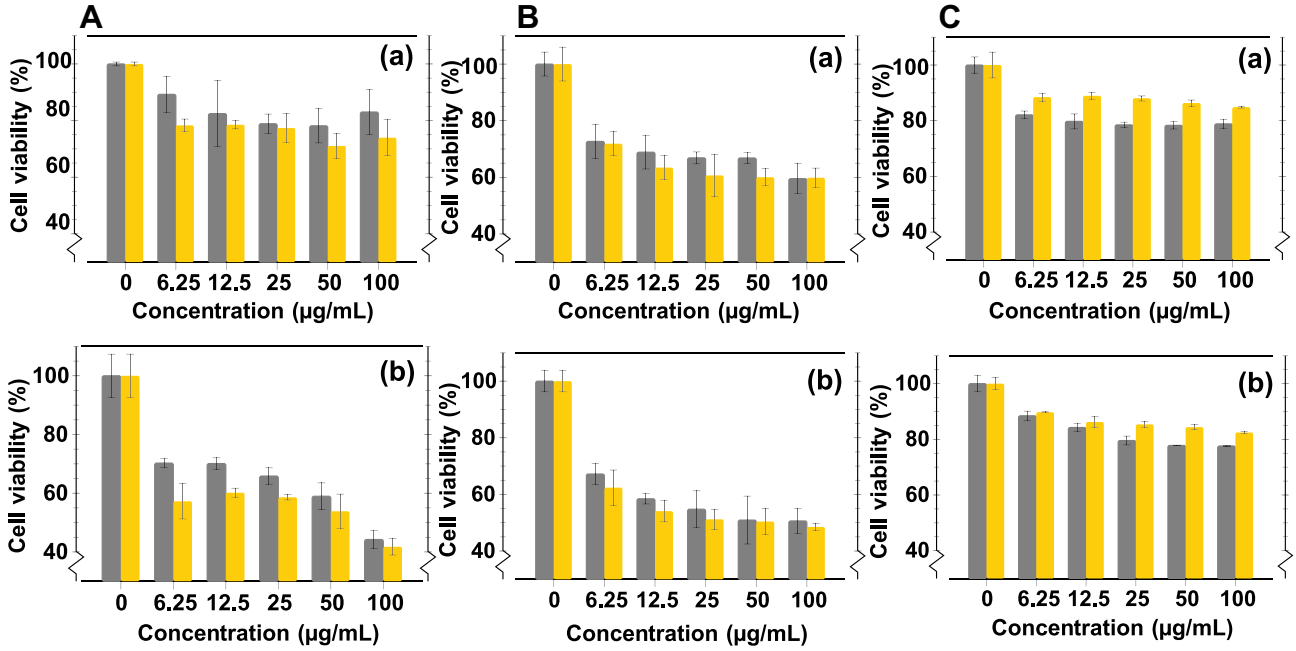

Figure 7 Cellular viabilities of (**A**) PC-3 and (**B**) LNCaP cancer cells and (**C**) HAECs normal cells after treating with AuNPs-WSCS (gray histogram) and AuNPs-WSCS-DOTA-BBN (yellow histogram) for (a) 24 and (b) 48 h.

h.[66] Previous studies have also suggested that with the peptide targeted- and drug loaded-AuNPs, the cytotoxicity effects toward the cancer cells can be enhanced.

In the current investigations, we have shown that, even without drug loading, the viability of PC-3 and LNCaP cells remained at ~70% and ~60% when treated with AuNPs-WSCS-DOTA-BBN (ca. 25 μg/mL) at 24 h. Additional data from previous investigations include the IC_{50} of the curcumin-functionalized gold nanoparticles (cur-AuNPs) which was found to be 280 μg/mL against PC-3 cells at 24 h.[67]

Overall, our investigations suggest that BBN conjugated on AuNPs-WSCS-DOTA-BBN exerts significant targeting effects on GRP receptors overexpressed on PC-3 and LNCaP cells. It is also noteworthy that the cytotoxicity effects, as observed on prostate carcinoma cells, for both AuNPs-WSCS-DOTA-BBN and AuNPs-WSCS, without any drug loading, may provide new avenues in cancer therapy.

Cytotoxicity Studies of AuNPs Against Non-Cancerous Cells

The cytotoxicity of AuNPs-WSCS and AuNPs-WSCS-DOTA-BBN (50 μg/mL) was also evaluated using HAEC cells—a non-cancerous cell line under in vitro conditions using MTT assays. Cell viability results of HAECs after treating with AuNPs-WSCS (gray color) and AuNPs-WSCS-DOTA-BBN (yellow color) for 24 and 48 h are shown in Figure 7C. Compared with cancer cells (PC-3 and LNCaP), HAEC cells showed significant higher cell viability. The HAECs viability still remained almost 80–90% even at concentrations as high as 100 μg/mL. At 24 h, HAEC cells showed 78–82% and 85–89% viability after treating with AuNPs-WSCS and AuNPs-WSCS-DOTA-BBN within the concentrations of range of 12.5–100 μg/mL (Figure 7C(a)). When we increased the incubation time to 48 h, cell viabilities of HAECs remained almost identical with 78–88% and 82–90% for AuNPs-WSCS and AuNPs-WSCS-DOTA-BBN, respectively (Figure 7C(b)). These results suggest that normal metabolic adaptation to cell growth and cell proliferation of HAECs normal cells occur under the AuNPs environment even with increasing incubation times. Besides, during cancer cell progression, cancer cells show characteristic changes in their metabolic profiles for their adenosine triphosphate (ATP) requirement, such as increased uptake rate of glucose to survive and multiply under the cancer microenvironment.[68] It is also important to note that the repeating unit of CS has a chemical motif, composed of glucosamine units, which mimic the glucose structure. This may explain why the AuNPs-WSCS and AuNPs-WSCS-DOTA-BBN exhibit efficient cellular uptake in the cancer cells than the normal cells.[69] Consequently, the CS carrier function may bring about higher cellular uptake of the AuNPs leading to higher cytotoxicity to the cancer cells. Additional data from the previous literature also supports our observation.

AuNPs prepared in aqueous WSCS solutions also promoted cell proliferation of human skin fibroblast CRL 2522 cells.[17] Similarly, Au nanostructures did not show significant cytotoxicity effects on HAECs and normal mouse fibroblasts (L929) cell lines.[70,71] Regarding the BBN targeting peptide, the HAECs normal cell viability, treated with AuNPs-WSCS-DOTA-BBN, was found to be higher as compared to AuNPs-WSCS. This observation may suggest that the BBN conjugate not only enhances cytotoxicity of AuNPs toward the PC-3 and LNCaP cancerous cells but might also help in diminishing the cytotoxicity of AuNPs toward the HAECs normal cells.

Finally, we have also investigated the cytotoxic effects of polymeric templates WSCS and WSCS-DOTA-BBN, without the gold nanoparticles, toward cancerous and normal cells. Figure 8 shows cell viability of the PC-3 and LNCaP cancerous cells and HAECs normal cells after treating with polymer templates (WSCS and WSCS-DOTA-BBN) for 24 and 48 h. Post treatment, the PC-3, LNCaP and HAEC cells still showed high viability of up to >80%, even after exposures at the high concentrations of 100 μg/mL, for both WSCS and WSCS-DOTA-BBN (Figure 8A(a-b), 8B(a-b), and 8C(a-b)), respectively. In sharp contrast, as discussed above, the gold nanoparticulate analogs, AuNPs-WSCS-DOTA-BBN, showed significantly higher cytotoxicity to both cancer cells as compared with AuNPs-WSCS. It is also noteworthy that the cytotoxicity differences between WSCS and WSCS-DOTA-BBN were not statistically significant. These cytotoxicity results agree with previous reports which suggest that the CS exhibited non- or minimal toxicity, thus making it a safe nanomaterial in drug delivery.[72] CS causes no hemolysis of red blood cells (<10%) over 1–5 h with CS in the molecular weight ranges of <5 kDa, 5–10 kDa, and >10 kDa at concentrations of up to 5 mg/mL.[73]

Our results, as discussed above, provide credible evidence that the BBN conjugation with WSCS-DOTA-BBN results in reduced toxicity of the final AuNPs-WSCS-

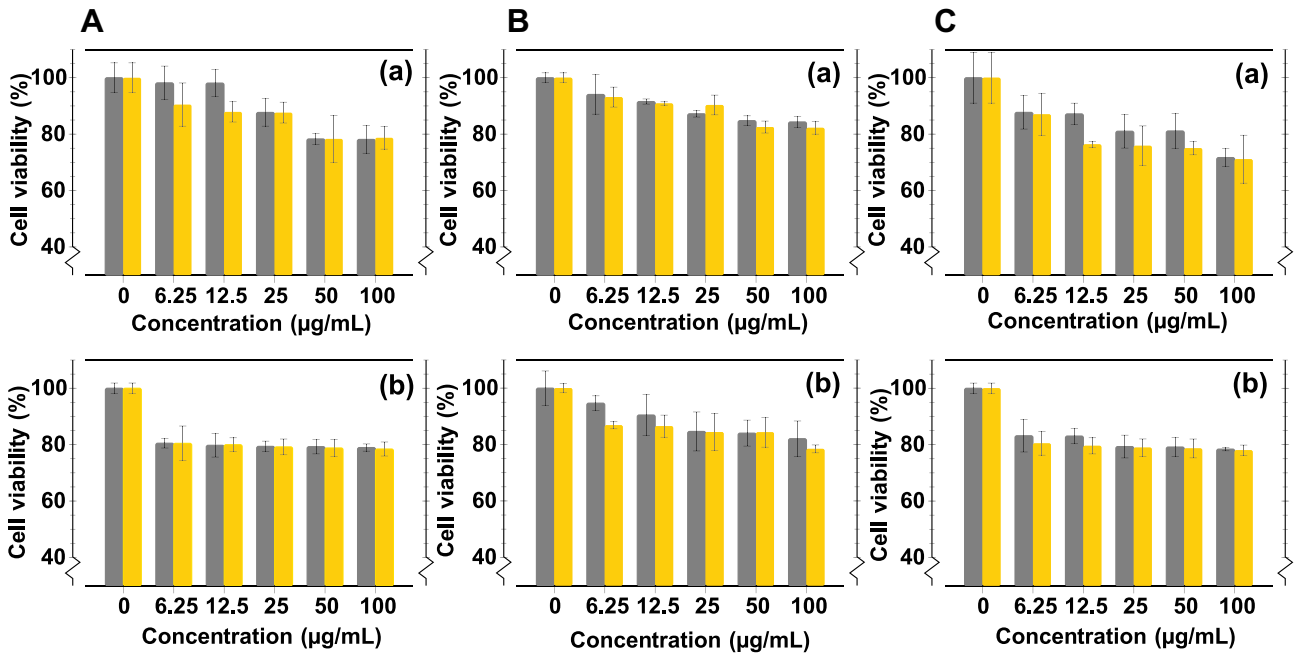

Figure 8 Cellular viabilities of (**A**) PC-3 and (**B**) LNCaP cancer cells and (**C**) HAECs normal cells after treating with WSCS (gray histogram) and WSCS-DOTA-BBN (yellow histogram) for (a) 24 and (b) 48 h.

DOTA-BBN conjugate toward normal cells due to the targeting function of the BBN peptide.

Conclusions

The growing importance of functionalized AuNPs in molecular imaging and therapy requires the development of tumor cell-specific hybrid AuNPs. In this context, our approach toward the development of multifunctional AuNPs-WSCS-DOTA-BBN conjugate, as elaborated in this paper, is an important advance in furthering the biomedical applications of hybrid gold nanoparticles. This paper also validates our overarching objective toward the creation of tumor cell-targeted AuNPs-WSCS-DOTA-BBN as evidenced through agonistic interactions with GRP receptors which are over-expressed in prostate tumors (Figure 6 and S7). Although the utility of chitosan as a nano template is well known, our investigations provide unprecedented experimental pathways in harnessing the realistic potential of water-soluble chitosan nanoparticles, as carriers of both AuNPs as well as targeted bombesin peptide—all rendering prostate tumor cell specificity for the AuNPs-WSCS-DOTA-BBN nanomedicine agent for use in molecular imaging and therapy.

Acknowledgments

The authors W.P and K.V.K gratefully acknowledge the Coordinated Research Project (CRP, No. 18316), International Atomic Energy Agency (IAEA), United Nation, Vienna (Austria) for research financial and DOTA-BBN peptide supports. The author (T.T.) acknowledges the Ministry of Higher Education, Science, Research and Innovation for a graduate scholarship. We also appreciate the Center of Radiation Processing for Polymer Modification and Nanotechnology (CRPN) at Kasetsart University (Thailand) (Under THA1010, THA1011, THA 1014 under IAEA Technical Cooperation Programme), for facilities support. We also extend our appreciation to Office of Atom for Peace (OAP) (Thailand) and Synchrotron Light Research Institute (Thailand) for irradiation and some analytical service. K.V.K thanks the University of Missouri-Columbia and the Green Nanotechnology Institute within the Medical School for providing all the research logistics and facilities for undertaking joint collaborations with the United Nations IAEA, W.P and T.T.

Disclosure

The authors report no conflicts of interest in this work.

References

1. Khoobchandani M, Katti KK, Karikachery AR, et al. New approaches in breast cancer therapy through green nanotechnology and nano-ayurvedic medicine – pre-clinical and pilot human clinical investigations. *Int J Nanomed*. 2020;15:181. doi:10.2147/IJN.S219042
2. Khoobchandani M, Katti KK, Karikachery AR, Thipe VC, Bloebaum PLR, Katti KV. Targeted phytochemical-conjugated gold nanoparticles in cancer treatment. In: *Biotechnology Products in Everyday Life Springer*. 2019;37–52.

3. Chanda N, Kattumuri V, Shukla R, et al. Bombesin functionalized gold nanoparticles show in vitro and in vivo cancer receptor specificity. *Proc Natl Acad Sci*. 2010;107(19):8760–8765.
4. Silindir-Gunay M, Karpuz M, Ozturk N, Ozer AY, Erdogan S, Tuncel M. Radiolabeled, folate-conjugated liposomes as tumor imaging agents: formulation and in vitro evaluation. *J Drug Deliv Sci Technol*. 2019;50:321–328.
5. Wang L, Chen Y, Lin HY, et al. Near-IR-absorbing gold nanoframes with enhanced physiological stability and improved biocompatibility for in vivo biomedical applications. *ACS Appl Mater Interfaces*. 2017;9(4):3873–3884.
6. Ginzburg AL, Truong L, Tanguay RL, Hutchison JE. Synergistic toxicity produced by mixtures of biocompatible gold nanoparticles and widely used surfactants. *ACS Nano*. 2018;12(6):5312–5322.
7. Pedrosa P, Vinhas R, Fernandes A, Baptista PV. Gold nanotheranostics: proof-of-concept or clinical tool? *Nanomaterials*. 2015;5 (4):1853–1879.
8. Zhang Y, Qian J, Wang D, Wang Y, He S. Multifunctional gold nanorods with ultrahigh stability and tunability for in vivo fluorescence imaging, SERS detection, and photodynamic therapy. *Angewandte Chemie Int Ed*. 2013;52(4):1148–1151.
9. Chhour P, Naha PC, Cheheltani R, Benardo B, Mian S, Cormode DP. Gold nanoparticles for biomedical applications: synthesis and In vitro evaluation. *Nanomater Pharmacol*. 2016;87–111.
10. Li X, Takashima M, Yuba E, Harada A, Kono K. PEGylated PAMAM dendrimer–doxorubicin conjugate-hybridized gold nanorod for combined photothermal-chemotherapy. *Biomaterials*. 2014;35 (24):6576–6584. doi:10.1016/j.biomaterials.2014.04.043
11. Chanda N, Kan P, Watkinson LD, et al. Radioactive gold nanoparticles in cancer therapy: therapeutic efficacy studies of GA-198AuNP nanoconstruct in prostate tumor–bearing mice. *Nanomedicine*. 2010;6 (2):201–209. doi:10.1016/j.nano.2009.11.001
12. Katti KV. Renaissance of nuclear medicine through green nanotechnology: functionalized radioactive gold nanoparticles in cancer therapy—my journey from chemistry to saving human lives. *J Radioanalytical Nucl Chem*. 2016;309(1):5–14. doi:10.1007/s10967-016-4888-0
13. Katti KV, Khoobchandani M, Thipe VC, et al. Prostate tumor therapy advances in nuclear medicine: green nanotechnology toward the design of tumor specific radioactive gold nanoparticles. *J Radioanalytical Nucl Chem*. 2018;318(3):1737–1747. doi:10.1007/s10967-018-6320-4
14. Brown SD, Nativo P, Smith J-A, et al. Gold nanoparticles for the improved anticancer drug delivery of the active component of oxaliplatin. *J Am Chem Soc*. 2010;132(13):4678–4684. doi:10.1021/ja908117a
15. Takahashi F, Yamamoto N, Todoriki M, Jin J. Sonochemical preparation of gold nanoparticles for sensitive colorimetric determination of nereistoxin insecticides in environmental samples. *Talanta*. 2018;188:651–657.
16. Su L, Xiong Y, Chen Z, et al. MoO3 nanosheet-assisted photochemical reduction synthesis of Au nanoparticles for surface-enhanced Raman scattering substrates. *Sens Actuators B Chem*. 2019;279:320–326.
17. Piroonpan T, Katemake P, Pasanphan W. Comparative study of different chitosan solutions to assist the green synthesis of gold nanoparticles under irradiation. *Rad Phys Chem*. 2020;169:108250.
18. Gamal-Eldeen AM, Moustafa D, El-Daly SM, et al. Gum Arabic-encapsulated gold nanoparticles for a non-invasive photothermal ablation of lung tumor in mice. *Biomed Pharmacother*. 2017;89:1045–1054.
19. Gamal-Eldeen AM, Moustafa D, El-Daly SM, et al. Photothermal therapy mediated by gum Arabic-conjugated gold nanoparticles suppresses liver preneoplastic lesions in mice. *J Photochem Photobiol B*. 2016;163:47–56.
20. Thakkar KN, Mhatre SS, Parikh RY. Biological synthesis of metallic nanoparticles. *Nanomedicine*. 2010;6(2):257–262.
21. Gao X, Zhang Y, Zhao Y. Biosorption and reduction of Au (III) to gold nanoparticles by thiourea modified alginate. *Carbohydr Polym*. 2017;159:108–115.
22. Pasanphan W, Rattanawongwiboon T, Choofong S, Güven O, Katti KK. Irradiated chitosan nanoparticle as a water-based antioxidant and reducing agent for a green synthesis of gold nanoplatforms. *Rad Phys Chem*. 2015;106:360–370.
23. Wongkrongsak S, Tangthong T, Pasanphan W. Electron beam induced water-soluble silk fibroin nanoparticles as a natural antioxidant and reducing agent for a green synthesis of gold nanocolloid. *Rad Phys Chem*. 2016;118:27–34.
24. Jr NP B, Go LP, Querebillo CJ, Hildebrandt P, Limpoco FT, Enriquez EP. Controlled microwave-hydrolyzed starch as a stabilizer for green formulation of aqueous gold nanoparticle ink for flexible printed electronics. *ACS Appl Nano Mater*. 2018;1 (3):1247–1256.
25. Pu S, Li J, Sun L, Zhong L, Ma Q. An in vitro comparison of the antioxidant activities of chitosan and green synthesized gold nanoparticles. *Carbohydr Polym*. 2019;211:161–172.
26. Pasanphan W, Chirachanchai S. Conjugation of gallic acid onto chitosan: an approach for green and water-based antioxidant. *Carbohydr Polym*. 2008;72(1):169–177.
27. Pasanphan W, Buettner GR, Chirachanchai S. Chitosan gallate as a novel potential polysaccharide antioxidant: an EPR study. *Carbohydr Res*. 2010;345(1):132–140.
28. Yuan J-F, Zhang Z-Q, Fan Z-C, Yang J-X. Antioxidant effects and cytotoxicity of three purified polysaccharides from Ligusticum chuanxiong Hort. *Carbohydr Polym*. 2008;74(4):822–827.
29. Li J, Du Y, Liang H. Low molecular weight water-soluble chitosans: preparation with the aid of cellulase, characterization, and solubility. *J Appl Polym Sci*. 2006;102(2):1098–1105.
30. Murugadoss A, Chattopadhyay A. A 'green' chitosan–silver nanoparticle composite as a heterogeneous as well as micro-heterogeneous catalyst. *Nanotechnology*. 2007;19(1):015603.
31. Huang H, Yang X. Synthesis of chitosan-stabilized gold nanoparticles in the absence/presence of tripolyphosphate. *Biomacromolecules*. 2004;5(6):2340–2346.
32. Karra SR, Schibli R, Gali H, et al. 99mTc-labeling and in vivo studies of a bombesin analogue with a novel water-soluble dithiadiphosphine-based bifunctional chelating agent. *Bioconjug Chem*. 1999;10(2):254–260.
33. Nock B, Nikolopoulou A, Chiotellis E, et al. [99mTc]Demobesin 1, a novel potent bombesin analogue for GRP receptor-targeted tumour imaging. *Eur J Nucl Med Mol Imaging*. 2003;30(2):247–258.
34. Pujatti PB, Massicano AVF, Mengatti J, de Araújo EB. Preparation of [In-111]-labeled-DTPA-bombesin conjugates at high specific activity and stability: evaluation of labeling parameters and potential stabilizers. *Appl Radiat Isot*. 2012;70(5):856–863.
35. Hohne A, Mu L, Honer M, et al. Synthesis, 18F-labeling, and in vitro and in vivo studies of bombesin peptides modified with silicon-based building blocks. *Bioconjug Chem*. 2008;19(9):1871–1879.
36. Yang Y-S, Zhang X, Xiong Z, Chen X. Comparative in vitro and in vivo evaluation of two 64Cu-labeled bombesin analogs in a mouse model of human prostate adenocarcinoma. *Nucl Med Biol*. 2006;33 (3):371–380.
37. Aranda-Lara L, Ferro-Flores G, Azorín-Vega E, et al. Synthesis and evaluation of Lys1 (α, γ-Folate) Lys3 (177Lu-DOTA)-Bombesin (1-14) as a potential theranostic radiopharmaceutical for breast cancer. *Appl Radiat Isot*. 2016;107:214–219.
38. Hajiramezanali M, Atyabi F, Mosayebnia M, et al. 68Ga-radiolabeled bombesin-conjugated to trimethyl chitosan-coated superparamagnetic nanoparticles for molecular imaging: preparation, characterization and biological evaluation. *Int J Nanomedicine*. 2019;14:2591.

39. Mendoza-Nava H, Ferro-Flores G, FdM R, et al. 177Lu-dendrimer conjugated to folate and bombesin with gold nanoparticles in the dendritic cavity: a potential theranostic radiopharmaceutical. *J Nanomater*. 2016;2016.
40. Kulhari H, Kulhari DP, Singh MK, Sistla R. Colloidal stability and physicochemical characterization of bombesin conjugated biodegradable nanoparticles. *Colloids Surf a Physicochem Eng Asp*. 2014;443:459–466.
41. Kongkaoroptham P, Piroonpan T, Hemvichian K, Suwanmala P, Rattanasakulthong W, Pasanphan W. Poly (ethylene glycol) methyl ether methacrylate-graft-chitosan nanoparticles as a biobased nanofiller for a poly (lactic acid) blend: radiation-induced grafting and performance studies. *J Appl Polym Sci*. 2015;132:37.
42. Vo KDN, Guillon E, Dupont L, Kowandy C, Coqueret X. Influence of Au (III) interactions with chitosan on gold nanoparticle formation. *J Phys Chem C*. 2014;118(8):4465–4474.
43. Vo KDN, Kowandy C, Dupont L, Coqueret X. Evidence of chitosan-mediated reduction of Au (III) to Au (0) nanoparticles under electron beam by using OH and e- aq scavengers. *Chem Commun*. 2015;51(19):4017–4020.
44. Petroski JM, Wang ZL, Green TC, El-Sayed MA. Kinetically controlled growth and shape formation mechanism of platinum nanoparticles. *J Phys Chem B*. 1998;102(18):3316–3320.
45. Chen Y, Gu X, Nie C-G, Jiang Z-Y, Xie Z-X, Lin C-J. Shape controlled growth of gold nanoparticles by a solution synthesis. *Chem Commun*. 2005;(33):4181–4183.
46. Balasubramani G, Ramkumar R, Raja RK, Aiswarya D, Rajthilak C, Perumal P. Albizia amara Roxb. mediated gold nanoparticles and evaluation of their antioxidant, antibacterial and cytotoxic properties. *J Cluster Sci*. 2017;28(1):259–275.
47. Heidari Z, Sariri R, Salouti M. Gold nanorods-bombesin conjugate as a potential targeted imaging agent for detection of breast cancer. *J Photochem Photobiol B*. 2014;130:40–46.
48. Khandelia R, Jaiswal A, Ghosh SS, Chattopadhyay A. Gold nanoparticle–protein agglomerates as versatile nanocarriers for drug delivery. *Small*. 2013;9(20):3494–3505.
49. Keshvari F, Bahram M, Farshid AA. Gold nanoparticles biofunctionalized (grafted) with chiral amino acids: a practical approach to determining the enantiomeric percentage of racemic mixtures. *Anal Methods*. 2015;7(11):4560–4567.
50. Paciotti GF, Myer L, Weinreich D, et al. Colloidal gold: a novel nanoparticle vector for tumor directed drug delivery. *Drug Deliv*. 2004;11(3):169–183.
51. Rivera-Gil P, Jimenez De Aberasturi D, Wulf V, et al. The challenge to relate the physicochemical properties of colloidal nanoparticles to their cytotoxicity. *Acc Chem Res*. 2013;46(3):743–749.
52. Kannan R, Rahing V, Cutler C, et al. Nanocompatible chemistry toward fabrication of target-specific gold nanoparticles. *J Am Chem Soc*. 2006;128(35):11342–11343.
53. Honer M, Mu L, Stellfeld T, et al. 18F-labeled bombesin analog for specific and effective targeting of prostate tumors expressing gastrin-releasing peptide receptors. *J Nucl Med*. 2011;52(2):270–278.
54. Rogers BE, Bigott HM, McCarthy DW, et al. MicroPET imaging of a gastrin-releasing peptide receptor-positive tumor in a mouse model of human prostate cancer using a 64Cu-labeled bombesin analogue. *Bioconjug Chem*. 2003;14(4):756–763.
55. Zhang E, Xing R, Liu S, Qin Y, Li K, Li P. Advances in chitosan-based nanoparticles for oncotherapy. *Carbohydr Polym*. 2019;222:115004.
56. Nativo P, Prior IA, Brust M. Uptake and intracellular fate of surface-modified gold nanoparticles. *ACS Nano*. 2008;2(8):1639–1644.
57. Nagasaki S, Nakamura Y, Maekawa T, et al. Immunohistochemical analysis of gastrin-releasing peptide receptor (GRPR) and possible regulation by estrogen receptor βcx in human prostate carcinoma. *Neoplasma*. 2012;59(2):224–232.
58. Dozmorov MG, Hurst RE, Culkin DJ, et al. Unique patterns of molecular profiling between human prostate cancer LNCaP and PC-3 cells. *The Prostate*. 2009;69(10):1077–1090.
59. Ischia J, Patel O, Bolton D, Shulkes A, Baldwin GS. Expression and function of gastrin-releasing peptide (GRP) in normal and cancerous urological tissues. *BJU Int*. 2014;113:40–47.
60. Levi J, Sathirachinda A, Gambhir SS. A high-affinity, high-stability photoacoustic agent for imaging gastrin-releasing peptide receptor in prostate cancer. *Clin Cancer Res*. 2014;20(14):3721–3729.
61. Baratto L, Jadvar H, Iagaru A. Prostate cancer theranostics targeting gastrin-releasing peptide receptors. *Mol Imaging Biol*. 2018;20(4):501–509.
62. Richter S, Wuest M, Bergman CN, Krieger S, Rogers BE, Wuest F. Metabolically stabilized 68Ga-NOTA-Bombesin for PET imaging of prostate cancer and influence of protease inhibitor phosphoramidon. *Mol Pharm*. 2016;13(4):1347–1357.
63. Nafee N, Schneider M, Schaefer UF, Lehr C-M. Relevance of the colloidal stability of chitosan/PLGA nanoparticles on their cytotoxicity profile. *Int J Pharm*. 2009;381(2):130–139.
64. Guo J, O' Driscoll CM, Holmes JD, Rahme K. Bioconjugated gold nanoparticles enhance cellular uptake: a proof of concept study for siRNA delivery in prostate cancer cells. *Int J Pharm*. 2016;509(1–2):16–27.
65. Shiao Y-S, Chiu -H-H, Wu P-H, Huang Y-F. Aptamer-functionalized gold nanoparticles as photoresponsive nanoplatform for co-drug delivery. *ACS Appl Mater Interfaces*. 2014;6(24):21832–21841.
66. Kim D, Jeong YY, Jon S. A drug-loaded aptamer-gold nanoparticle bioconjugate for combined CT imaging and therapy of prostate cancer. *ACS Nano*. 2010;4(7):3689–3696.
67. Nambiar S, Osei E, Fleck A, Darko J, Mutsaers AJ, Wettig S. Synthesis of curcumin-functionalized gold nanoparticles and cytotoxicity studies in human prostate cancer cell line. *Appl Nanosci*. 2018;8(3):347–357.
68. Fadaka A, Ajiboye B, Ojo O, Adewale O, Olayide I, Emuowhochere R. Biology of glucose metabolization in cancer cells. *J Oncol Sci*. 2017;3(2):45–51.
69. Uldry M, Ibberson M, Hosokawa M, Thorens B. GLUT2 is a high affinity glucosamine transporter. *FEBS Lett*. 2002;524(1–3):199–203.
70. Gu C, Wu H, Ge G, et al. In vitro effects of hollow gold nanoshells on human aortic endothelial cells. *Nanoscale Res Lett*. 2016;11(1):1–10.
71. Dhamecha D, Jalalpure S, Jadhav K. Nepenthes khasiana mediated synthesis of stabilized gold nanoparticles: characterization and biocompatibility studies. *J Photochem Photobiol B*. 2016;154:108–117.
72. Kean T, Thanou M. Biodegradation, biodistribution and toxicity of chitosan. *Adv Drug Deliv Rev*. 2010;62(1):3–11.
73. Richardson SW, Kolbe HJ, Duncan R. Potential of low molecular mass chitosan as a DNA delivery system: biocompatibility, body distribution and ability to complex and protect DNA. *Int J Pharm*. 1999;178(2):231–243.